Check for updates

Investigating the relationship between COVID-19 shutdown and land surface temperature on the Anatolian side of Istanbul using large architectural impermeable surfaces

Lutfiye Kusak[1] · Ufuk Fatih Kucukali[2]

Abstract

Artificial impermeable surfaces are becoming more prevalent, especially in urban areas, as a result of shifting land use and cover, roads, roofs, etc. The modification of land surface temperature (LST) can also be accomplished through artificially impermeable surfaces. Large artificial impermeable surfaces, such as rooftops, parking lots, and other areas of use, can be found in industrial zones, shopping malls, industrial airports, and other locations. For the Anatolian side of Istanbul, 14 Landsat 8 OLI/TIRS imagery images over the years 2016–2022 were investigated. To evaluate how well the study's images could be utilized, correlation and cosine similarity approaches were employed. A total of 12 images may be employed for research LST studies, it was discovered. We looked at closure dates during the COVID-19 epidemic to find out how human migration affected the LST. In addition, the LST value was estimated using the ordinary least squares (OLS) method employing LST and other biophysical indices. A decrease in LST values was seen as a result of the investigation. High levels of similarity and correlation were found between the images used. Results from the Google Mobility Index also provide support to the study. All of these facts provide support to Istanbul's Anatolian side experiencing lower surface temperature values, which consequently affects the city's massive structures.

Keywords LST · OLS · COVID-19 · Large architectural impermeable surfaces · Cosine similarity · Correlation

✉ Lutfiye Kusak
lutfiyekusak@mersin.edu.tr

Ufuk Fatih Kucukali
ufkucukali@aydin.edu.tr

[1]   Department of Geomatics Engineering, Mersin University, Mersin, Turkey

[2]   Department of Architecture, Istanbul Aydın University, Istanbul, Turkey

🖄 Springer

1 Introduction

The virus outbreak, which began in December 2019 in Wuhan, China's Hubei area, and attacked the respiratory system, spread as quickly as January 2020. SARS-CoV-2 is the name given to this virus. In the future, virus cases in various nations in Europe, North America, and Asia–Pacific began to be reported, and the World Health Organization declared a global epidemic on March 11, 2020. It was announced on March 13, 2020, that Europe has now become the epicenter of the coronavirus crisis. There are 762,791,152 confirmed coronavirus cases worldwide as of April 12, 2023. Unfortunately, 6,897,025 patients died as a result of the infection (WHO, 2023). COVID-19 spreads through the air when humans breathe in droplets and small airborne particles containing the virus. As a result, several limits have been imposed to reduce human mobility, particularly in highly populated areas, and to control the spread of COVID-19.

Workplace closures in many nations, including Turkiye, provide services in a home office environment, online continuing education, suspension of intercity and international transportation, and restrictions outside specific hours to satisfy personal requirements. These restrictions were imposed in Turkiye following the WHO's announcement of COVID-19, a global epidemic (RG, 2020). The Turkish COVID-19 pandemic timeline is shown in Fig. 1.

While full restrictions were set on weekends, partial closure practices were carried out between 19:00 and 05:00 for fault in some periods and sometimes between 09:00PM and 05:00AM hours from the night (Tan, 2022).
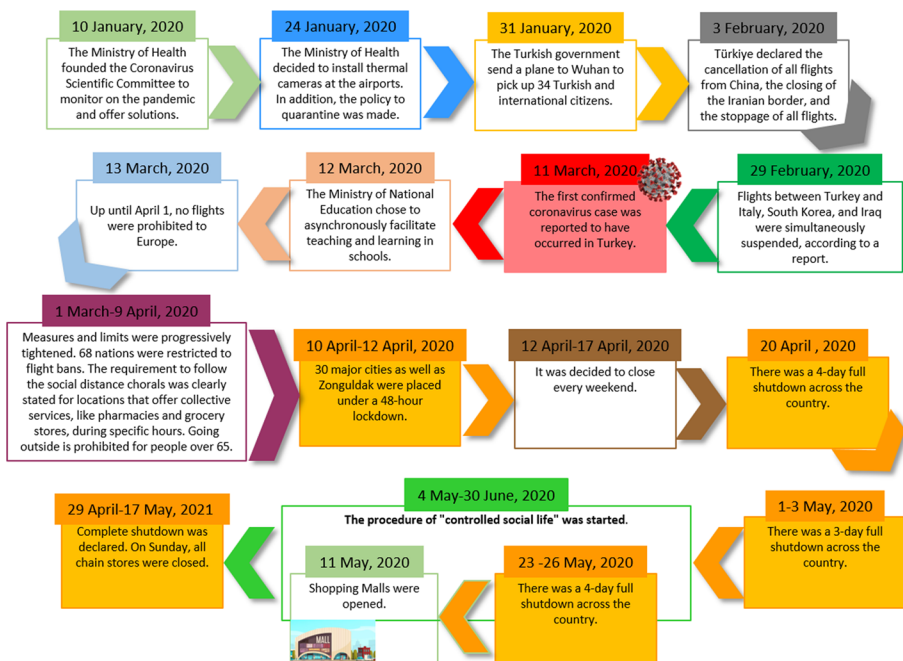

Fig. 1 Timeline of the COVID-19 pandemic in Türkiye

Numerous countries and localities studies have been conducted to demonstrate both the positive and negative impacts of the COVID-19 pandemic. Following the WHO's declaration of the pandemic, numerous countries, including Turkiye, imposed various restrictions. The effects of these restrictions on mobility are investigated. At the scale of Istanbul, new patterns of human mobility (Başeğmez & Aydın, 2021) have evolved that differ from the traditional conditions in parks, transit stations, workplaces, groceries, pharmacies, and residential areas (Arik & Çavdaroğlu, 2023). The limits have resulted in numerous negative and positive investigations. Negative social and economic problems have occurred. The restrictions had a negative impact on the health and education sectors, as well as the production, entertainment, food, and tourism sectors. Because Istanbul is Turkiye's most populous province, and any negative situations that arise will have an impact on the entire country, fragility maps and reports on the scale of districts and neighborhoods have been revealed under the headings of social, settlement, and economy for the province of Istanbul 2020 (Bimtaş, 2020). Furthermore, the use of masks and gloves, if necessary, suggested by WHO for all those who do not work in the health sector, in addition to those who do work in the health sector, has resulted in environmental contamination. Furthermore, the unplanned increase in water use for hygiene purposes resulted in a loss of water resources (Balçik et al., 2021).

Some positive results occurred as a result of the limits imposed to prevent the spread of the epidemic. Restrictions, home office applications in companies, online education systems in education, and traffic density dropped, while favorable results in air quality (Kotan & Erener, 2022) appeared owing to the reduction of industrial activity. To uncover these findings, investigations covering short, medium, and long time periods were conducted around the world and in Turkiye. The months of March and April are covered by short-term applications (El et al., 2021; Şahin, 2020; Teufel et al., 2021). Mid-term applications were used for the months of March, April, and May (Baysan et al., 2021), whereas long-term applications (Efe, 2022) were used for the months of January through August of the whole year. To establish comparisons and assess their correctness, all applications were supplied with data prior to 2020, and it was found that Google Mobility and Apple Mobility Change data were also preferred in the research. In addition to a single city, the studies looked at PM_{10}, $PM_{2.5}$, NO_2, CO, SO_2, and O_3 particle levels in multiple cities, countries, and around the world. While local measuring stations can provide particle data, satellite images such as Sentinel and MODIS were favored for obtaining data such as PM_{10} and $PM_{2.5}$. There are situations in practically all publications where the traffic density of these pollutants, for example, decreases from 50–100% for Istanbul to 10–20% (Şahin, 2020), and it has been determined that this is related to a decrease in industrial activities.

Many research has been conducted on the LST (Guha & Govil, 2020) and the factors that influence it. LST is detected via satellites, drones, and airplanes equipped with thermal sensors. According to the investigations, 68.39% of Landsat satellite images were used and determined. In the investigations, correlation, regression, descriptive statistics, and machine learning approaches are most commonly used. Among the factors influencing LST are topological features, building standards, city morphology, land use, low vegetation density, building design, size, roof characteristics, city size, air temperature, night lights, heat-emitting sources such as industrial and transportation, as well as wind, wind speed, and land surface conditions (Almeida & Cl, 2021). In addition to these factors, numerous research on the effects of an emergency, such as COVID-19, on the LST has been undertaken. As a consequence of the short-term studies conducted around the world, the April and May periods were examined, and increases in air quality and decreases in surface temperatures were noted in cities in general (El et al.,

2021). In another study, when Landsat 8 OLI/TIRS images were reviewed in April and May, it was discovered that the surface temperature value declined significantly more than in previous periods, and the explanation for this was attributed to the low concentration level of vehicles and population on the roads. The reduction in vehicle traffic and industrial pollutants, in particular, had a substantial impact on Raipur City's LST values during the shutdown time. Furthermore, NDVI values increased during this era as compared to previous periods (Guha & Govil, 2021). LST values were shown to be decreasing in the study supported by the Google mobility index report. The LST values between 2015 and 2020 were analyzed during the days between April and May in the study, which demonstrated that the air quality indicators improved, and decreases in the LST values were detected during the study's closing periods (Chakraborty et al., 2021; Venter et al., 2021). Images from Landsat TM5, Landsat OLI/TIRS, and Landsat MODIS taken between the years 2000 and 2020 were used in a research for the Iranian city of Esfahan. The findings show that during the COVID-19 shutdown period, heat stress in the area decreased (Roshan et al., 2022). The analysis done for Tehran looked at a much wider time frame, from 1995 to 2020. Analyses of land use were conducted, and UHI changes were identified. Investigations have been done into how the closures of COVID-19 may affect these areas (Roshan et al., 2021).

Some of the studies conducted period a significantly longer time period. These researches tracked not just the months of March, April, and May, but also the entire year. Bacak and colleagues evaluated SO_2, NO_x, CO, lead, hydrocarbon, particulate matter, and O_3 concentrations in the Istanbul scale. When the O_3 level reached in June, the temperature values increased as well. This indicates the average ozone concentration is affected by both temperature and human activity. Because human activity has dropped throughout the pandemic, the O_3 concentration has also decreased, resulting in temperature drops. Reductions in NO_2 levels and other pollutants were observed as a result of the limits (Bacak et al., 2020). The effect of reducing traffic density owing to COVID-19 limits on urban temperature was explored in research undertaken by Teufel et al. in 2021, validating this article. The seasons January–May 2020 and April–May 2020 were investigated. As a result of the study, 1 degree decreases in areas near major traffic zones were detected, with traffic decreasing by 80% (Teufel et al., 2021). Sentinel 5P data for NO_2 and MODIS data for AOD and LST were utilized in the study for the Northern Emirates of the United Arab Emirates (NEUAE). They used data from March to June of 2019 and 2020. NO_2, AOD, and SUHII levels were found to be lower (Alqasemi et al., 2021). Taoufik et al., 2021 employed Landsat 8 OLI/TIRS long-term data from 2016 to 2020. When the average values were examined, it was discovered that the LST averages at Morocco dropped during the COVID-19 period (Taoufik et al., 2021). The impacts of changes in human activities on urban temperature were investigated, as well as the most effective means of establishing the relationship between them. Landsat images, building information, and easyGO location service data were used. Images from the 2019/12/7 open period, the 2020/02/09 closed period, the 2018/0/08 open period, and the 2020/0/13 post-closing period were used. Furthermore, OLS values derived from the Modified Normalized Difference Water Index (MNDWI), the Normalized Difference Built-up Index (NDBI), and population density (PD) were compared. The ordinary least squares (OLS) linear regression model was used to examine and compare different elements' contributions to the urban thermal environment (Cai et al., 2021).

Furthermore, the correlations used in this study to reveal the relationship of the data with each other are among the highly reversed methodologies. During the COVID-19 period, correlation is utilized to assess the links between population changes and urban

thermal environment changes (Cai et al., 2021), LST's NDVI (Guha & Govil, 2021), NDBI, and air quality (Alqasemi et al., 2021).

In the study, cosine similarity, another supportive method preferred for detecting the similarity of LST values, is mostly preferred in text mining, though deep learning applications in which images are analyzed (Dhyani & Pandya, 2021) and the similarity of images to each other is investigated (Ahn et al., 2023; Uzkent et al., 2019), where land surface changes are detected (Lee et al., 2021).

Using 14 different time images of the Anatolian side of Istanbul, it was examined in this study to see if the COVID-19 closure had any impact on the land surface temperature. The surface temperatures of the area were assessed in this study, as they were in all the others, but unlike the others, it also paid attention to large impermeable architectural structures that had to be idle for a specific amount of time due to COVID-19 restrictions because of the intense human mobility. In this approach, it was possible to examine whether these structures indeed had a different LST feature from other structures and to attempt to demonstrate the effect of COVID-19 on the LST. Firstly, using the 2018 CLC dataset, the LULC structure of the study area was examined. Then, 14 images' LST maps were created. The southern shoreline of the Anatolian side, where the settlement area is dense, was chosen as the sub-study area in order to reduce the impact of the cloud effect on the surface temperatures of some images. The correlations between 14 images were examined, and their cosine similarities were determined, using the LST pixel values in this region. These evaluations led to the choice to use 12 images. Predicted LSTs were also derived using biophysical factors to assist the study, and graphs were made based on the land uses between LSTs and their correlations were assessed. Large impermeable structures in the sub-study area have received LST examinations, and it has been discussed if COVID-19 limits have an impact on the surface temperature data of these structures.

2 Material and methods

This section introduces the work area, the datasets used, and the method's work flowchart (Fig. 2) within the context of the study. There are two primary stages of the research. The first stage involved picking the study area, explaining why it was chosen, presenting the data and its pre-processing, the second stage involved methods.

2.1 Study area

Geographically, Istanbul's eastern section, also referred to as the Anatolian Side, is located on the Asian continent and is located east of the Bosphorus. There are 38 districts in Istanbul, 14 of which are on the Anatolian side. Istanbul has a climate that is close to the Mediterranean, humid subtropical, and oceanic, according to Köppen and Trewartha. The climate is dominated by the Mediterranean, particularly on the southern shores of the Anatolian side. In Pendik, which is on the south coast of the area being studied and is inside the study region, the average April and May temperature and precipitation values were 12.4 degrees, 16.8 degrees, and 55.9 mm, 52 mm, respectively. In this case, the inner-most city of Üsküdar's average April and May temperatures and precipitation totals are 11.3 degrees and 15.8 degrees, respectively, and 45 and 37 mm, respectively. The typical temperature and precipitation totals in Ile, which is located on the Black Sea coast, are 11.2 degrees, 15.2 degrees, 61.1 mm, and 54.3 mm, respectively, in April and May.
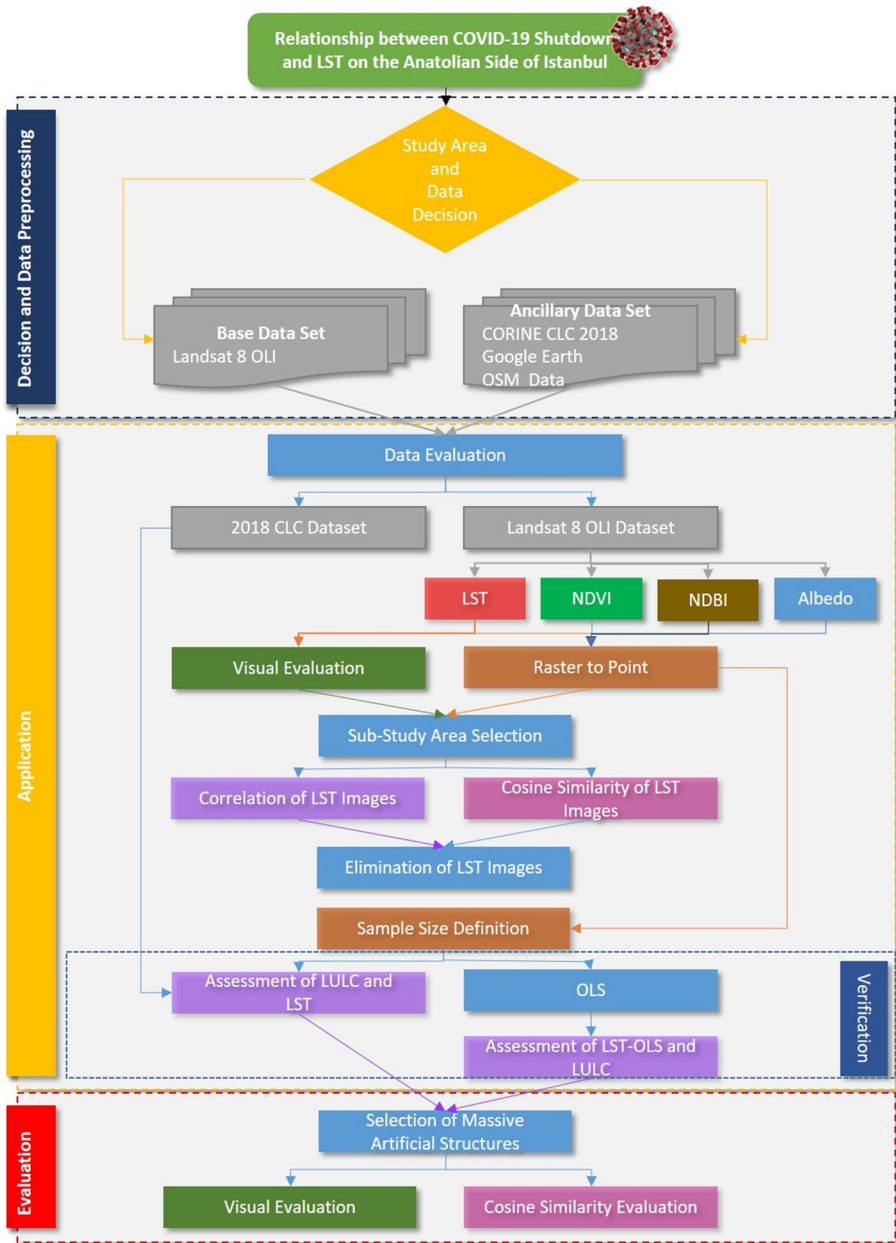
Fig. 2 Flowchart of the study

Due to the city's rapid urbanization growth, the Anatolian Side of Istanbul has been examined because there are more impervious surfaces there. Istanbul Airport, which enables international travel like Sabiha Gokcen Airport on this side, is one of the most vital distribution and logistics hubs. Due to recent migrations and development, 2019
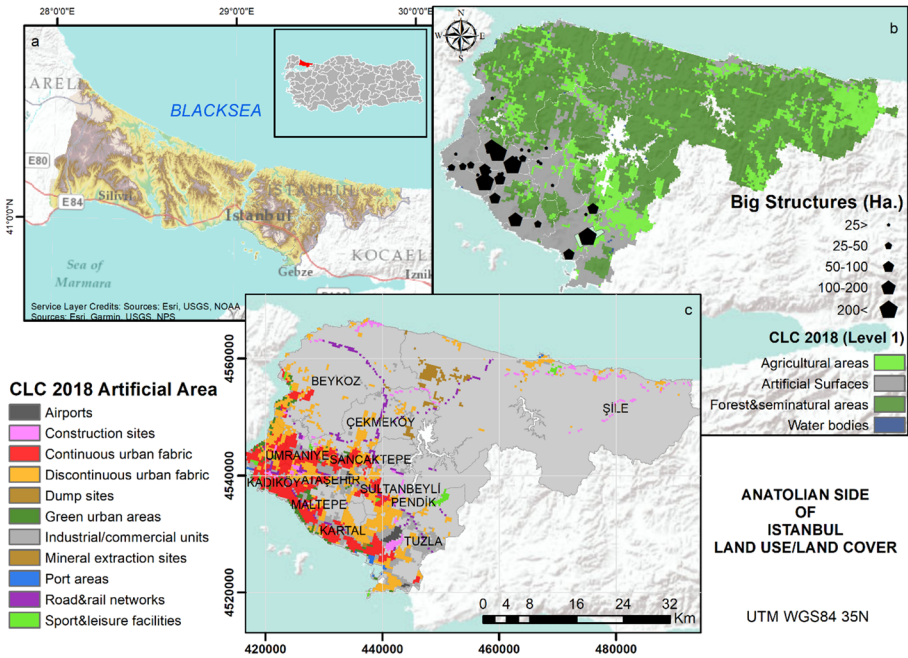
Fig. 3 Anatolian Side of Istanbul CORINE Land Cover (2018)

projections indicate that the population of the Anatolian Side has reached 4.3 million. This region is residence to one-third of Istanbul's population.

As a result of the population growth, there are more residential areas and other places, such shopping centers. Due to urbanization and large structures, the area, which was previously mostly made up of green spaces, has experienced a rise in impermeable surfaces (Fig. 3).

In specifically on the Anatolian side, which is a main accumulation area in terms of placement options for these massive structures, there were significant changes in the use of commercial and residential functions throughout the COVID-19 shutdown. This urban area has been researched in order to assess the main hypothesis and supporting hypotheses of the study.

2.2 Datasets

2.2.1 CORINE data as ancillary data

The CORINE Land Cover (CLC) dataset from 2018 was utilized in the study to show the current state of the research area and the correlation between LST and land use. The European Union played a role in the creation of the CORINE dataset, which was used for the first time in 1990 to define the land cover. The resolution varies depending on which dataset was used to build it, and these datasets were created using satellite images and base maps. The CORINE dataset is divided into five primary categories: artificial surfaces,

agricultural, forest and semi-natural areas, wetlands, and water bodies (György Büttner et al., 2021; Kosztra et al., 2017).

2.2.2 Remote sensing and weather data

The study's main dataset consists of Landsat 8 OLI/TIRS satellite images. As a result of the preliminary analysis, 15 images were obtained on the Earth Explorer site. One of these images, nevertheless, was canceled because the research region was too cloudy. The 14 remaining pictures had all been prepared for analysis. The before COVID-19 shutdown period, during the COVID-19 shutdown period, and the after COVID-19 shutdown period are all taken into account in the images. The dates were carefully considered when collecting these images, and they were also grouped among themselves. There should be no more than 8 days between dates, it was observed. Instead of expressing the dataset used in the study with dates, the abbreviation name was used (Table 1).

Unfortunately, as seen in Table 1, there are only 9 images with less than 10% cloud cover. The ratio is high in other images. The images were nevertheless analyzed despite the fact that the cloud cover on the Anatolian side, which is the study area, is less than on the other European side.

In this study, LST, NDVI, NDBI, and albedo values of the study area were determined using Landsat 8 OLI/TIRS images (Table 1). Using QGIS 3.14, all Landsat images were prepared, clipped, and then LST, NDVI, NDBI, and albedo data were calculated for each date.

Three main variables may affect LST variation: season, hour of the day, and land-use circumstances. The effects of the other two elements must be kept to a minimum in order to evaluate the LST variation only connected with changes in land-use circumstances. Images obtained in the same location will have identical local times since the Landsat satellite orbits around the sun synchronously. Unfortunately, the satellite transit time in Istanbul is approximately 8:30 am. As a result, the LST does not reflect midday results but rather morning results. In a while, they are regarded as acceptable for the study taking into account the warming and cooling results of their structures.

For the validation and verification of the acquired satellite images, the data on the ground temperature at the time of the Landsat 8 OLI/TIRS satellite's transit are crucial (Avdan & Jovanovska, 2016; Gallo et al., 2011; Jiang & Lin, 2021; Mukherjee & Singh, 2020). For this reason, temperature values from seven local weather stations were used to validate and confirm the temperatures found in satellite images (Table 1). The Turkish State Meteorological Service, which is connected to the Ministry of Environment, Urbanization, and Climate Change, provided meteorological parameters, including temperature data. As can be seen from the table, temperature measurements could not be made at some stations. However, these stations were not canceled because they were important for the study area.

2.2.3 Determination of large architectural structures

The 48 important building complexes, which spread a large region among artificial surfaces on the Anatolian side and include shopping malls, Modoko Furnishers Site, and Sabiha Gokcen Airport, have been digitalized using Google Earth Pro and visual interpretation (Fig. 2b). These fields were also checked with OSM data. The study focused on

Table 1 Landsat 8 OLI images of Istanbul and TSMS AWOS Station Temperature Values at 09:00 AM

Date		Cloud cover (%)			Temperature values (°C)						
	Abb	Land	Scene	Sile	Beykoz	Umraniye	Uskudar	Kadikoy	Pendik	Tuzla
Before	20,160,417	(La1)	0.34	0.09	26.5	N/A	N/A	N/A	22.2	23.6	N/A
	20,180,423	(Lb1)	0.16	0.13	24.3	17.7	20.4	21.8	N/A	20.6	21
	20,190,512	(Lc1)	6.22	1.42	17.8	21.3	23.3	22.6	21.6	21.1	23.6
	20,190,528	(Ld1)	0.66	3.12	22	24.8	N/A	N/A	29.4	28.9	31.9
During	20,200,412	(La2)	0.73	0.58	12	N/A	14.1	14.1	14.9	14.5	16.9
	20,200,428	(Lb2)	1.14	11.08	15	N/A	20.9	21.5	20.3	20.9	23.4
	20,200,514	(Lc2)	24.87	66.8	16.6	17.7	20.6	19	16.9	20.4	22.2
	20,200,530	(Ld2)	35.98	11.79	21.8	17.8	18.1	18.8	19	19.6	23.6
After	20,220,410	(La3)	12.37	17.06	22.8	17.4	20.2	19	19.8	19.4	21.8
	20,220,426	(Lb3)	22.89	35.53	25.4	17.8	20.1	20.2	19.1	21.9	21.6
	20,210,517	(Lc3)	16.13	4.66	16.2	19.6	22.1	20.8	23.7	23.5	22.2
	20,220,512	(Lc4)	1.17	2.61	23.1	21.6	21.5	21.8	19.2	21.8	22.3
	20,220,520	(Lc5)	0.09	0.04	17.9	19.2	19.3	20.3	20.5	19	21.1
	20,220,528	(Ld3)	7.71	11.75	24.1	26.4	28.4	28.7	27.9	28.3	29.4

TSMS: Turkish State Meteorological Service, AWOS: Automated Weather Observing System

the Modoko Furnishers Site, the Sabiha Gokcen Airport, and six shopping malls because of how large an area they cover. Due to the 900 square meter spatial resolution of each Landsat 8 OLI/TIRS satellite image pixel, only these 8 significant architectural structures could be used. Although Akasya and Ring Mall are smaller in size than other buildings, they were chosen specifically for their green roof feature. Meydan Mall is also chosen for the study because of the green roof type (Külekçi, 2017). Green roofs have been examined in the evaluation of UHI in studies (Baryła et al., 2019; Cao et al., 2020; Li et al., 2014; Sharifi & Lehmann, 2014; Sharma et al., 2016). In this study, it was examined whether it changed during the closure period and the change in LST value.

The number of pixels in the region drawn with the aid of Google Earth was used to calculate the size of the land used in the calculation. The results of the legal usage area are not reflected in it (Table 2). Their locations are shown in the study, and it is not intended to disparage their architectural achievements. In order to determine whether COVID-19 could be responsible for the temperature change, it was sought to examine locations with the highest levels of human activity.

2.3 Methods

2.3.1 Evaluation of the CLC dataset

In studies to ascertain land-use status, observe city change, and carry out LST and UHI assessments (Mashhoodi, 2020; Walawender et al., 2014), CLC dataset is widely employed as an additional dataset. For investigations on land classification, land surface change, and calculating emission values, the CLC dataset is preferred.

This study's objective was to evaluate the use and land cover on the Anatolian side, with a focus on artificial surfaces in particular. The CLC data collection divides artificial surfaces into four types (Table 3). Buildings, roads, or other man-made impermeable surfaces cover more than 80% of the continuous urban fabric areas, one of the urban fabric areas. When impermeable surfaces occupy between 30 and 80% of an area, the urban fabric has been deconstructed. Roads and railroads with a minimum width of 100 m are classed as roads/rail networks and related land, whereas all sorts of industrial and production centers, large shopping malls, research and development organizations, and power plants are considered to be industrial or commercial units. In addition, open mines, public facilities for disposing of industrial and mining waste, and building sites fall under this category. Zoos, cemeteries, stadiums, sports fields, golf courses, and urban biotope zones are all defined in the main title as artificial, non-agricultural vegetated places (Kosztra et al., 2017). Surface temperature values are influenced more by the urban fabric, industrial, commercial, and transportation facilities, as well as mines, landfills, and building sites, while artificial, non-agricultural vegetated areas have the opposite effect.

2.3.2 Evaluation of satellite images

For the research, satellite images were used to acquire additional biophysical metrics such as NDVI, NDBI, and albedo in addition to LST data.

Table 2 Large architectural structures examples

Name	Area (Ha)	Features	Google earth image	Name	Area (Ha)	Features	Google earth image
Rings mall	2.16	GR, SM, R		Akyaka Park Mall	11.88	SM, R	
Akasya mall	2.7	GR, SM, R		Icerenkoy Carrefour Mall	25.56	SM	
Viaport mall	6.66	SM, R		Modoko Furniture Site	22.68	IA, FS	
Meydan mall	25.56	GR, SM		Sabiha Gokcen Airport	927.45	Airport	

*GR: green roof, SM: shopping mall, R: residence, FS: furniture site, industrial area: IA

Table 3 CORINE land cover class names

1. Artificial Surfaces	
1.1 Urban fabric	1.3 Mine, dump and construction sites
1.1.1 Continuous urban fabric	*1.3.1 Mineral extraction sites*
1.1.2 Discontinuous urban fabric	*1.3.2 Dump sites*
1.2 Industrial, commercial and transport units	*1.3.3 Construction sites*
1.2.1 Industrial or commercial units	1.4 Artificial, non-agricultural vegetated areas
1.2.2 Road and rail networks and associated land	*1.4.1 Green urban areas*
1.2.3 Port areas	*1.4.2 Sport and leisure facilities*
1.2.4 Airports	
2. Agricultural areas	
3. Forest and seminatural areas	
4. Wetlands	
5. Water bodies	

2.3.2.1 NDVI The visible and near-infrared light reflected by vegetation is used to calculate the Normalized Difference Vegetation Index (NDVI). A healthy plant reflects far more near-infrared light, whereas an unhealthy plant reflects far less near-infrared light. Equation (1) is used to calculate the NDVI formula. Band 5 is near-infrared band (NIR), while Band 4 corresponds to red band.

$$\text{NDVI} = \frac{\text{NIR} - \text{RED}}{\text{NIR} + \text{RED}} \tag{1}$$

2.3.2.2 LST Images from satellites with thermal sensors, like Landsat, are used to derive LST values. Formulas related to LST calculation are given below (Liu & Zhang, 2011; Rongali et al., 2018; U.S. Geological Survey, 2019) for Landsat OLI/TIRS images. Each spectral band's image data from the Landsat Collections Level-1 products have been radiometrically and geometrically adjusted, and it is displayed as calibrated and quantized scaled digital numbers (DN). The format of the Landsat 8 OLI/TIRS data is as 8-bit and 16-bit unsigned integers, respectively. Using the radiometric rescaling coefficients available in the metadata file presented with the image product, Landsat Level-1 DN data can be scaled to Top of Atmosphere (TOA) spectral radiance ($L\lambda$) Eq. (2).

$$L\lambda = M_L \times Q_{\text{cal}} + A_L - O_i \tag{2}$$

where $L\lambda$ = Spectral radiance (W/ (m2 * sr * μm)). M_L = Radiance multiplicative scaling factor for the band (RADIANCE_MULT_BAND_10 from the metadata). A_L = Radiance additive scaling factor for the band (RADIANCE_ADD_BAND_10 from the metadata). Q_{cal} = Level 1-pixel value in DN.

Brightness temperature (BT) readings are used to determine the LST values. The TIRS band data should be converted from spectral radiance to brightness temperature (BT) using the thermal constants provided in the metadata file after the digital numbers (DNs) are converted to reflection Eq. (3).

$$\text{BT} = \frac{K_2}{\ln\left[(K_1/L\lambda) + 1\right]} - 273.15 \qquad (3)$$

where $L\lambda$ = TOA spectral radiance (Watts/ (m2 * srad * μm)). K_1= Band-specific thermal conversion constant from the metadata (K1_CONSTANT_BAND_10). K_2 = Band-specific thermal conversion constant from the metadata (K2_CONSTANT_BAND_10). In this study, K_1=1321.08 and K_2 = 777.89.

Using the following equation, Eq. (2), LST based on satellite brightness temperature (BT) was calculated (4). As a result, the study also defines emissivity values.

$$\text{LST} = \frac{\text{BT}}{1 + \left(\lambda + \frac{\text{BT}}{\alpha}\right)\ln\varepsilon} \qquad (4)$$

where BT is the effective at satellite temperature in Kelvin, λ is the wavelength of the emitted radiance in meters, $\alpha = 1.438 \times 10^{-2}$mK, and ε is the surface emissivity.

Studies have been carried out to obtain LST values using thermal bands (Cristóbal et al., 2018; Sobrino & Jiménez-Muñoz, 2005). The relationship between land cover and emissivity has been studied for many years since each object has an emissivity (Sobrino et al., 1990). Land cover classes and emissivity values have been determined, and NDVI-based studies have been conducted for the application of the derived values in satellite images (Malik et al., 2019; Stathopoulou et al., 2007).

For the purposes of this study, the LST calculation method created by Shen and employed in the prior study (Kusak & Kucukali, 2018) was preferred. In this case, emissivity values of 0.9923 are approved for water areas, 0.923 are allowed for urban impermeable and bare soil regions, and 0.986 are accepted for plant areas. For mixed regions, the formula in Eq. (5) is also employed (Shen et al., 2016).

$$\varepsilon = 1.00094 + 0.047\ln(\text{NDVI}) \qquad (5)$$

2.3.2.3 Albedo calculation A critical element that could be utilized to estimate the temperature of the ground surface is albedo. When considered generally, the reflected light is the sun's ray and varies depending on artificial or natural qualities. Albedo surfaces have the capacity to reflect electromagnetic energy falling on a surface. Numerous factors, including substance, color, the kind and characteristics of the soil or ground, hydrological structure, and content, are included in these features. Surface temperatures are significantly influenced by the surface albedo ratio (Firozjaei et al., 2019; Khorrami & Gunduz, 2020; Oh et al., 2020; Zaeemdar & Baycan, 2017; Y. Zhou et al., 2012). Albedo reflections vary based on the roof materials, the surface, and subsurface temperatures, and studies have shown that impermeable surfaces have a greater surface temperature but a lower albedo value (Lee et al., 2015; Trlica et al., 2017; Zhao et al., 2015). Numerous research has examined the impact of high albedo, the usage of light-colored roof and wall paints, as well as the characteristics of urban areas (Guerri et al., 2021) on the LST value (Jacobson and Ten Hoeve 2012; Liu et al., 2017).

The average quantity of sunlight reflected is displayed. TOA readings are used in the calculation of albedo. Using satellite sensors, the algorithm series was developed to calculate albedo (Liang et al., 2003). In this work, albedo values were determined by applying the Landsat 7 normalized formula to the OLI bands of Landsat 8 OLI/TIRS at Eq. (6).

$$\alpha = \frac{0.356\rho_2 + 0.130\rho_4 + 0.373\rho_5 + 0.085\rho_6 + 0.072\rho_7 - 0.0018}{1.016} \tag{6}$$

where ρ_2 is Band 2 (blue), ρ_4 is Band 4 (red), ρ_5 is Band 5 (near-infrared (NIR)), ρ_6 is Band 6 (shortwave ınfrared (SWIR) 1), ρ_7 is Band 7 (shortwave ınfrared (SWIR) 2).

The albedo value is between 0 and 1. It has values of 0.18 in areas with broad-leaved plants, 0.16 in areas with conifers, 0.12 in areas with dry soil, 0.15 in areas with moist soil, 0.25 in areas with grass, and 0.15 in areas with asphalt surfaces, 0.55 in areas with new structures on concrete surfaces, and 0.20 in areas with older structures (Guerri et al., 2021; Trlica et al., 2017; Zaragoza & Bartolom, 2012).

2.3.2.4 NDBI Normalized Difference Built-up Index (NDBI) is used for obtaining the structuring data. It ranges from -1 to 1 and is calculated using Eq. (7). Here Band 6 is SWIR1. If the result value approaches 1, information about buildings and impermeable surface is obtained.

$$NDBI = \frac{SWIR1 - NIR}{SWIR1 + NIR} \tag{7}$$

2.3.2.5 Sample size selection The study's sub-study region has a lot of pixels, which makes it difficult or impossible to do OLS calculations to validate the study in terms of land usage. As a result, the equation below was used to estimate how many samples should represent this location Eq. (8).

$$Sample\ size = \frac{\frac{z^2 * p * (1-p)}{e^2}}{1 + \left(\frac{z^2 * p * (1-p)}{e^2 * N}\right)} \tag{8}$$

where N is number of pixel study area, and e is margin of error and z is z-value in the equation. p is the sample proportion.

2.3.2.6 Correlation of values It is possible to examine the correlation between each pair of numerical variables in a dataset using a correlation matrix. It provides a brief summary of the entire dataset. It is more frequently used for exploratory than explanatory purposes. Correlation matrices were employed in some of the study's validation sections as a result. RStudio program was used to complete this process. The study was performed use of the GGally Package program libraries' ggcorr and ggpairs.

2.3.2.7 Cosine similarity The cosine similarity index calculates how similar two vectors in an inner product space are to one another. It establishes whether two vectors are roughly pointing in the same direction by calculating the cosine of the angle between them Eq. (9). In text mining, it is frequently employed. Studies are also done to find similarities in images.

$$D(x_m, x_j) = \cos(\theta) = \frac{\sum_{i=1}^{n} x_{mi} * x_{ji}}{\sqrt{\sum_{i=1}^{n} x_{mi}^2 * \sum_{i=1}^{n} x_{ji}^2}} \tag{9}$$

Cosine similarity was performed to both show and remove differences in the LST satellite images in order to validate the correlation results in the study. Also, this method was

selected in the study's results section during the review and assessment of massive artificial structures. MS Excel was used for cosine similarity calculations.

2.3.3 Ordinary least squares (OLS)

The OLS model was also used in the study to reveal the biophysical effects on the LST value. By incorporating dependent and independent variables, the OLS model (Charlton & Fotheringham, 2009; Scott & Janikas, 2010; Wheeler, 2014) is developed Eq. (10).

$$y_i = \beta_0 + \sum_k \beta_k x_k + \varepsilon \tag{10}$$

where y_i is dependent variables, β_0: intercept, β_k: estimated coefficient, x_k: the explanatory variable, ε: the random error.

Albedo, NDVI and NDBI are used as explanatory variables in the study, which used LST as dependent variables.

ArcGIS 10.5 was used for OLS operations.

2.3.4 Google Mobility Index

The Google Mobility Index dataset tracks daily visitor counts to various types of locations (such as supermarkets, parks, and railway stations) and compares them to baseline counts from days prior to the pandemic outbreak (Google, 2022). Baseline days are given as the median value throughout the five-week period from January 3rd to February 6th, 2020, and indicate a normal value for that day of the week. Because people apparently frequently have different habits on the weekends compared to weekdays, it is useful to measure it according to a usual value for that day of the week. Places divided six major groups. The category for groceries and pharmacies includes supermarkets, food distribution centers, farmers markets, specialized food stores, drug stores, and pharmacies. Public beaches, marinas, dog parks, plazas, and public gardens are examples of places that fall under the category of parks. Transit stations are locations where people provide public transportation, including subway, bus, and train stations. Restaurants, coffee shops, shopping malls, theme parks, museums, libraries, and movie theaters are all considered retail and recreation areas. areas where people live. Finally, places of employment are workplaces.

The index values of the districts of Ümraniye, Üsküdar, Ataşehir, and Pendik were analyzed because those districts contain the large architectural structures chosen for the study.

3 Results

Turkiye has implemented various safety precautions in response to the COVID-19 epidemic, just like the rest of the world. Regulations were among the measures put in place to limit people's mobility and prevent the spread of disease. In Turkiye, leaving the residence after a certain time is restricted, particularly between the beginning of April and the end of 2020 and on specific dates in May. Due to this, the research focused on April and May, and 14 Landsat 8 OLI/TIRS images were collected from EarthExplorer geoportal services.

LST values in the study area were assessed before, during, and after the COVID-19 shutdown. Before, during, and after the closure of COVID-19, LST values derived from Landsat images in the study area were assessed in order to determine how effectively the region and, particularly, major structures have restricted human mobility. The evaluation's findings are summarized in the part follows.

3.1 Evaluation of the CORINE dataset

Many studies have proven the impact of land use and cover on LST studies in particular. As a result, artificial surfaces in the study region are being investigated. The CLC 2018 dataset was used in the artificial area analysis.

Because of its expansion tendencies influenced by the transportation axis as well as its topographic and geomorphological structure, the Istanbul Metropolitan Region has a dense artificial surface structure in the east–west direction along the northern and southern coastlines. It is also becoming particularly widespread in newer satellite cities like Şile and Çekmeköy, which are situated on the northern coasts of Istanbul's Anatolian side and are expanding as urban peripheries (Fig. 3a).

The CLC dataset from 2018 was examined to show the status on artificial surfaces (Fig. 3c) in the research area on the Anatolian side (Table 4). Including The Prince Islands, 510,351 of the 1,805,625 pixels, obtained from CLC 2018 dataset, on the Anatolian side, around 28.3 percent of the area, are made up of artificial surfaces. Urban fabrics account for 55.89% of the artificial surfaces on the Anatolian Side, followed by industrial, commercial, and transportation infrastructures at 23.81% of the total area covered. Construction activities continue to change how spaces on these artificial surfaces are used, accounting for 9.26% of the total.

The Modoko Furniture Site and shopping malls that are the focus on the last part of the study are included in the CLC dataset's category of continuous urban structure, while Sabiha Gokçen Airport is classified under the category of transportation. In this study urban fabric is described as urban (U), ındustrial, commercial and transport units as industrial (I), mine, dump, construction sites and artificial, non-agricultural vegetated areas as other areas (O).

Table 4 Anatolian side CLC 2018 artificial surface percentage

CORINE artificial surfaces	%		%
1.1. Urban fabric	**55.89**	**1.3. Mine, dump and construction sites**	**14.74**
1.1.1. Continuous urban fabric	*23.60*	*1.3.1. Mineral extractionsites*	*5.44*
1.1.2. Discontinuous urban fabric	*32.29*	*1.3.2. Dumpsites*	*0.04*
1.2. Industrial, commercial and transport units	**23.81**	*1.3.2. Construction sites*	*9.26*
1.2.1. Industrial or commercial units	*17.40*	**1.4. Artificial, non-agricultural vegetated areas**	**5.56**
1.2.2. Road and rail networks and associated land	*4.91*	*1.4.1. Green urban areas*	*3.37*
1.2.3. Port areas	*0.35*	*1.4.2. Sport and leisure facilities*	*2.19*
1.2.4. Airports	*1.15*		
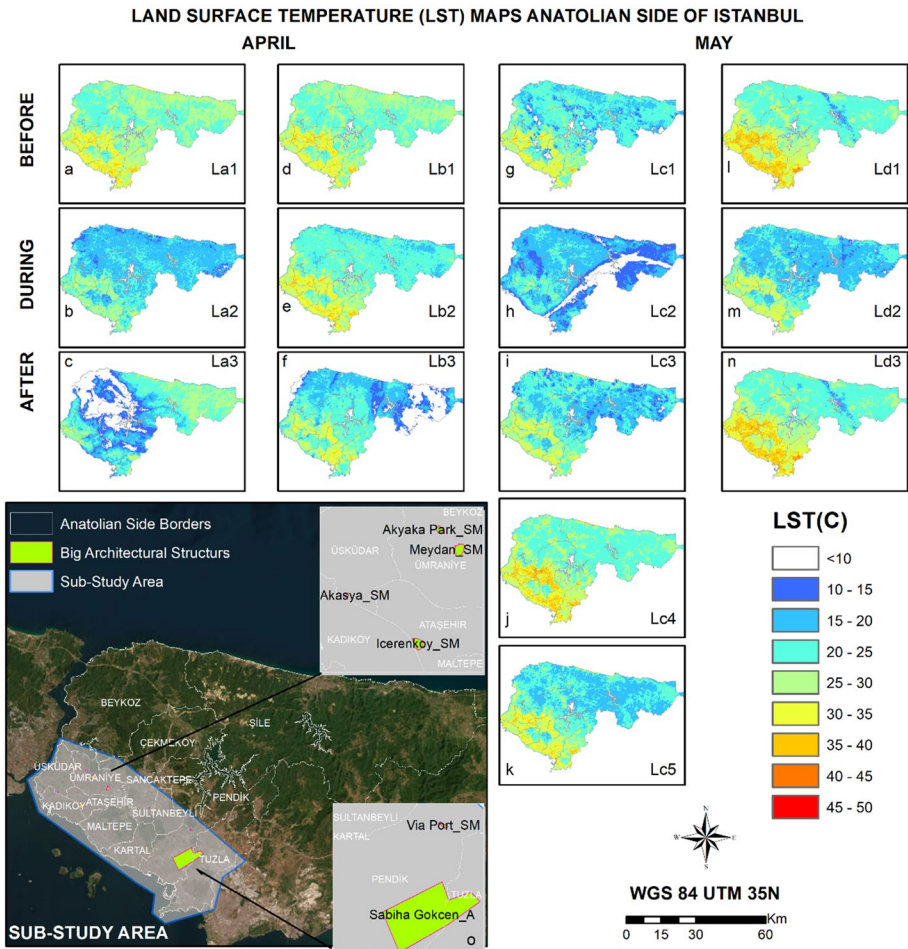
Fig. 4 LST images and sub-study area, **a** 17th April 2016 (La1), **b** 12th April 2020 (La2), **c** 10th April 2022 (La3) images are early April, **d** 23rd April 2018(Lb1), **e** 28th April 2020(Lb2), **f** 26th April 2022 (Lb3) images are late April, **g** 12th May 2019 (Lc1), **h** 14th May 2020 (Lc2), **i** 17th May 2021 (Lc3), **j** 12th May 2022 (Lc4), **k** 20th May 2022 (Lc5) images are early May, **l** 28th May 2019 (Ld1), **m** 30th May 2020 (Ld2), **n** 28th May 2022 (Ld3) images are late May in the study area, **o** sub-study area of Anatolian Side of Istanbul

3.2 LST evaluations of Anatolian side of Istanbul

The LST values derived via a total of 14 satellite images were examined in the study's second phase. Four of these images belong from before COVID-19 shutdown, four from during COVID-19 shutdown, and six from after COVID-19 shutdown (Fig. 4).

Figure 4a, d, h, and m is LST images from before COVID-19 closures, Fig. 4b, e, I, and m is LST images from COVID-19 shutdowns, and Fig. 4c, f, o, g, and l is LST images from the time after COVID-19 shutdowns.

To begin with, Landsat Band QA images were also investigated at in order to carry out the research correctly. In addition to the visual assessment in Fig. 4, band QA images also
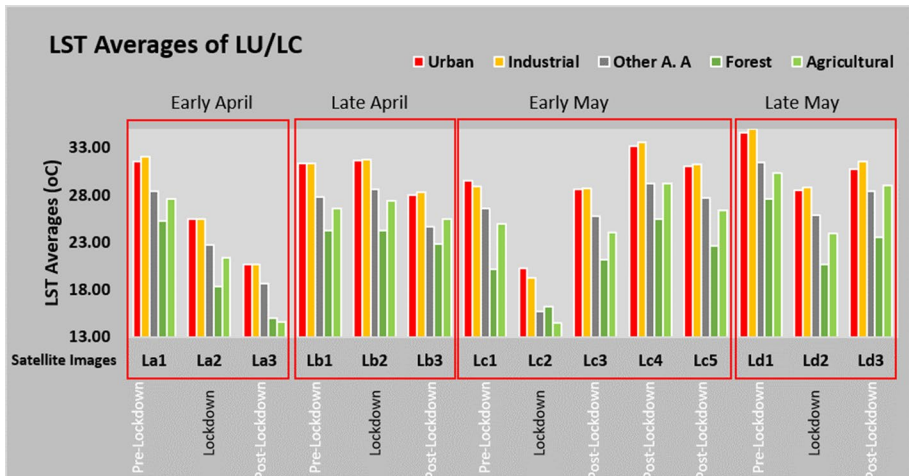
Fig. 5 LST averages of sub-study areas and LU/LC

indicate cloud activity, particularly in the northern and eastern regions of the Anatolian side of Istanbul. The surface temperatures in these areas are below 10 °C. Unusual low surface temperature values are found in Fig. 4b.

The Anatolian side of Istanbul has 2,064,866 pixels, gained via raster to point tools using ArcGIS. In the images stated above, clouds could be seen, particularly in the northern and eastern upper regions of Istanbul's Anatolian side. The massive impermeable architectural structures that serve as the basis for the study's inspiration were included in the sub-study area that was established in Istanbul's southern Anatolian region (Fig. 4o). The cloud impact is significantly less prominent here than it is elsewhere. As a result, a new sub-study region has been selected that includes big architectural buildings where clouds are less effective and hence surface temperature measurements are less affected. This region's pixel number is 514,676.

With a total of 514,676 pixels, the CLC dataset of the research region was used to compute the land-use distribution. Their calculations show that it is made up of areas that are 48.93% urban, 20.49% industrial, 5.68% other artificial area, 16.76% forest, and 8.14% agricultural.

The graph below was created by averaging the LST values of the images (Fig. 5). When the graph is inspected, it is clear that, with the exception of the Lb2 shutdown period, the average LST values of the other shutdown periods fell in all land uses and land coverings.

A graph of LST values and variations in urban, industrial, and other regions has been generated in addition to the average values in order to analyze the LST distributions in artificial surface areas in greater detail (Fig. 6).

When the LST distributions of artificial surfaces are studied, they are shown to be normal distributions. Except for the Lc1 image, temperatures in the images before the COVID-19 shutdown ranged between 25 and 35 degrees Celsius. Except for Lb2, concentrations were recorded in the 20–30 range during the COVID-19 shutdown periods. Except for the La3 image, a distribution at 20–40 25–35 degrees is observed after the COVID-19 closure, as it was before the closure.

The evaluation results from Landsat 8 OLI/TIRS were also compared with data from TSMS for 7 different stations in the study to validate the data (Table 5). As a result,
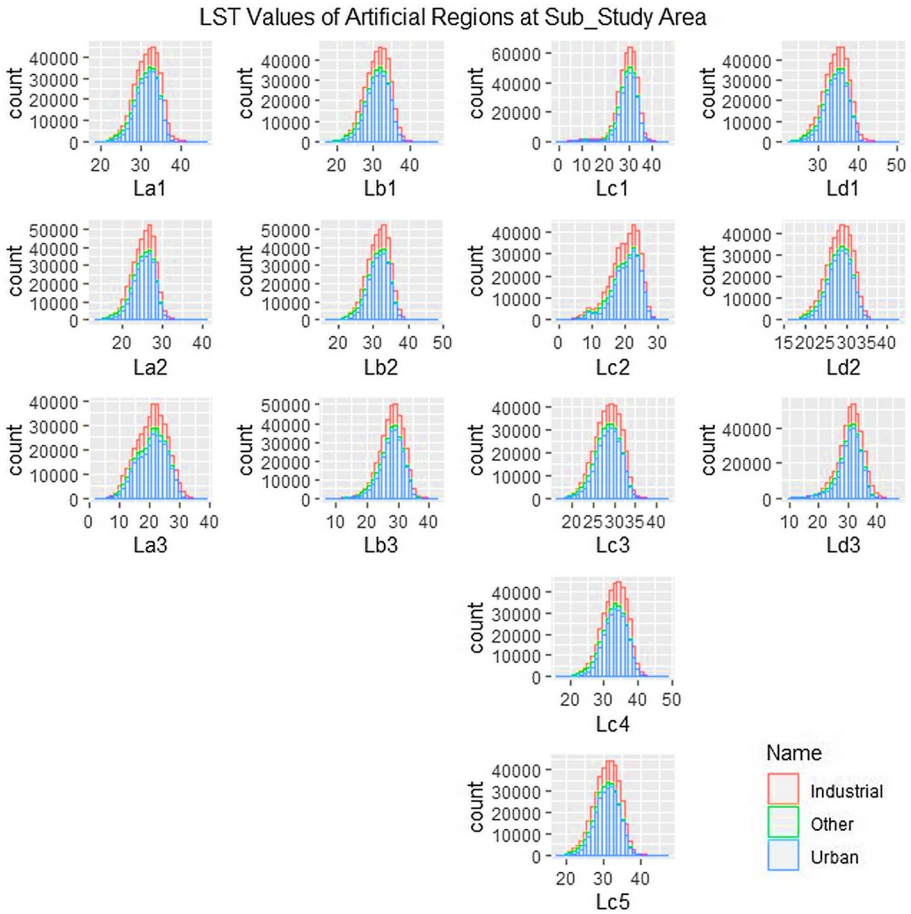
Fig. 6 LST values of artificial regions at sub-study area

outcomes from the ground observation data at 9:00 a.m. and the LST values were assessed. On a few dates, data could not be retrieved. The lack of data on these dates could be explained by missing records at the observation sites. There were 98 findings when differences between TSMS data and LST values were evaluated as absolute. These disparities are distributed as follows: <2 °C, 2–5 °C, 5–7 °C, 7–9 °C, 9–11 °C, >11 °C 25.51%, 27.55%, 16.33%, 13.27%, 5.10%, 3.06%, respectively. Furthermore, N/A values account for 9.18% of these data. The differences between the local measurements and the LST assessments in the analyzed sources can reach up to 8–10 degrees depending on the land surface's usage and cover condition (Avdan & Jovanovska, 2016; Do Nascimento et al., 2022). In addition, different climatic zones and different land covers make a difference between LST values and meteorological station measurements (Martin et al., 2019). Seasonal circumstances and daytime nighttime (Sekertekin & Bonafoni, 2020) can contribute to such variations. Unfortunately, the low spatial resolution of satellite images acquired using thermal cameras must also be considered in the investigations. The LST value of 0.3 degree from the Lc3 image at Beykoz suggests the presence of a cloud at the relevant station. However, when viewed in aggregate, there is little difference between TSMS data and LST values.

Table 5 TSMS AWOS Station Temperature, LST values, Differences, and Standard Deviation of the Anatolian Side of Istanbul

Data		TSMS AWOS station temp (°C) (9:00 AM)							LST Values (°C) of AWOS Stations (8:45 AM)						
		Sile	Beykoz	Umraniye	Uskudar	Kadikoy	Pendik	Tuzla	Sile	Beykoz	Umraniye	Uskudar	Kadikoy	Pendik	Tuzla
Before	(La1)	26.5	N/A	N/A	N/A	22.2	23.6	N/A	25.9	21.2	26.7	26.3	27.1	31.5	33.9
	(Lb1)	24.3	17.7	20.4	21.8	N/A	20.6	21	25.2	21.9	25.3	25.9	25.8	28.9	28.1
	(Lc1)	17.8	21.3	23.3	22.6	21.6	21.1	23.6	20.5	21.3	23.4	25.3	25.3	28.8	29.7
	(Ld1)	22	24.8	N/A	N/A	29.4	28.9	31.9	23.3	24.0	30.1	28.1	31.6	34.5	34.3
During	(La2)	12	N/A	14.1	14.1	14.9	14.5	16.9	16.1	16.7	18.6	21.1	21.3	23.6	25.4
	(Lb2)	15	N/A	20.9	21.5	20.3	20.9	23.4	19.2	21.8	25.4	27.7	27.2	32.1	31.1
	(Lc2)	16.6	17.7	20.6	19	16.9	20.4	22.2	13.7	15.7	18.8	18.2	16.9	12.2	14.4
	(Ld2)	21.8	17.8	18.1	18.8	19	19.6	23.6	19.6	18.3	24.3	23.9	24.0	27.6	28.7
After	(La3)	22.8	17.4	20.2	19	19.8	19.4	21.8	21.3	12.7	24.4	24.3	24.4	27.3	27.4
	(Lb3)	25.4	17.8	20.1	20.2	19.1	21.9	21.6	23.8	8.0	11.9	21.6	21.9	21.4	20.0
	(Lc3)	16.2	19.6	22.1	20.8	23.7	23.5	22.2	17.9	0.3	23.0	23.3	24.1	30.2	20.7
	(Lc4)	23.1	21.6	21.5	21.8	19.2	21.8	22.3	24.1	22.3	26.8	26.9	27.2	32.9	31.6
	(Lc5)	17.9	19.2	19.3	20.3	20.5	19	21.1	20.0	20.7	23.5	25.2	27.2	29.5	31.4
	(Ld3)	24.1	26.4	28.4	28.7	27.9	28.3	29.4	22.2	18.8	26.3	26.2	28.4	33.9	34.1
Data		Differences (°C)							Standard Dev						
		Sile	Beykoz	Umraniye	Uskudar	Kadikoy	Pendik	Tuzla	Sile	Beykoz	Umraniye	Uskudar	Kadikoy	Pendik	Tuzla
Before	(La1)	0.6	N/A	N/A	N/A	-4.9	-7.9	N/A	0.5	N/A	N/A	N/A	3.4	5.6	N/A
	(Lb1)	-0.9	-4.2	-4.9	-4.1	N/A	-8.3	-7.1	0.7	2.9	3.5	2.9	N/A	5.9	5.0
	(Lc1)	-2.7	0.0	-0.1	-2.7	-3.7	-7.7	-6.1	1.9	0.0	0.1	1.9	2.6	5.5	4.3
	(Ld1)	-1.3	0.8	N/A	N/A	-2.2	-5.6	-2.4	1.0	0.6	N/A	N/A	1.6	3.9	1.7
During	(La2)	-4.1	N/A	-4.5	-7.0	-6.4	-9.1	-8.5	2.9	N/A	3.2	4.9	4.5	6.4	6.0
	(Lb2)	-4.2	N/A	-4.5	-6.2	-6.9	-11.2	-7.7	3.0	N/A	3.2	4.4	4.9	7.9	5.5
	(Lc2)	2.9	2.0	1.8	0.8	0.0	8.2	7.8	2.1	1.4	1.2	0.6	0.0	5.8	5.5
	(Ld2)	2.2	-0.5	-6.2	-5.1	-5.0	-8.0	-5.1	1.5	0.3	4.4	3.6	3.5	5.6	3.6

Table 5 (continued)

Data		Differences (°C)							Standard Dev						
		Sile	Beykoz	Umraniye	Uskudar	Kadikoy	Pendik	Tuzla	Sile	Beykoz	Umraniye	Uskudar	Kadikoy	Pendik	Tuzla
After	(La3)	1.5	4.7	−4.2	−5.3	−4.6	−7.9	−5.6	1.0	3.3	3.0	3.8	3.3	5.6	4.0
	(Lb3)	1.6	9.8	8.2	−1.4	−2.8	0.5	1.6	1.1	6.9	5.8	1.0	2.0	0.3	1.1
	(Lc3)	−1.7	19.3	−0.9	−2.5	−0.4	−6.7	1.5	1.2	13.7	0.7	1.8	0.3	4.7	1.0
	(Lc4)	−1.0	−0.7	−5.3	−5.1	−8.0	−11.1	−9.3	0.7	0.5	3.8	3.6	5.7	7.9	6.6
	(Lc5)	−2.1	−1.5	−4.2	−4.9	−6.7	−10.5	−10.3	1.5	1.0	3.0	3.4	4.7	7.4	7.3
	(Ld3)	1.9	7.6	2.1	2.5	−0.5	−5.6	−4.7	1.3	5.4	1.5	1.8	0.3	4.0	3.3

Correlation of LST images   a

	La1	La2	La3	Lb1	Lb2	Lb3	Lc1	Lc2	Lc3	Lc4	Lc5	Ld1	Ld2	Ld3
La1	1													
La2	0.92	1												
La3	0.54	0.59	1											
Lb1	0.93	0.94	0.51	1										
Lb2	0.93	0.98	0.6	0.94	1									
Lb3	0.73	0.74	0.41	0.77	0.76	1								
Lc1	0.72	0.75	0.5	0.71	0.76	0.56	1							
Lc2	0.48	0.49	0.22	0.58	0.5	0.36	0.31	1						
Lc3	0.9	0.94	0.57	0.93	0.95	0.75	0.73	0.51	1					
Lc4	0.91	0.92	0.48	0.94	0.94	0.8	0.69	0.54	0.93	1				
Lc5	0.92	0.96	0.59	0.94	0.96	0.77	0.75	0.5	0.96	0.96	1			
Ld1	0.93	0.94	0.58	0.94	0.96	0.75	0.73	0.54	0.94	0.93	0.96	1		
Ld2	0.93	0.96	0.57	0.94	0.97	0.74	0.75	0.5	0.95	0.93	0.96	0.96	1	
Ld3	0.71	0.72	0.56	0.67	0.74	0.62	0.71	0.18	0.69	0.72	0.75	0.72	0.72	1

$R^2 = 0.9458$ (bar chart categories: <0.5, 0.5-0.7, 0.7-0.9, >0.9)

Cosine Similarity of LST images   b

	La1	La2	La3	Lb1	Lb2	Lb3	Lc1	Lc2	Lc3	Lc4	Lc5	Ld1	Ld2	Ld3
La1	1													
La2	3.72	1												
La3	13.4	12.8	1											
Lb1	2.87	3.19	13.6	1										
Lb2	2.91	2.07	12.8	2.61	1									
Lb3	5.94	6.34	14.6	5.56	5.72	1								
Lc1	8.42	7.91	14.3	8.44	7.97	10.1	1							
Lc2	12.2	12.3	18.5	11.4	12.1	13.5	15.3	1						
Lc3	3.71	3.03	13	3.1	2.78	6.06	8.23	12	1					
Lc4	3.43	3.45	13.9	2.82	2.81	5.29	8.68	11.4	3.19	1				
Lc5	3.47	2.63	12.8	3.01	2.41	5.94	7.92	12.2	2.34	2.5	1			
Ld1	2.59	3.52	13.1	2.65	2.4	5.68	8.4	11.8	3.22	3.04	2.96	1		
Ld2	3.53	2.5	12.9	3.15	2.35	6.28	7.95	12.2	2.65	3.25	2.37	3.1	1	
Ld3	6.84	7.07	13.2	7.35	6.56	8.05	8.48	15.5	7.2	6.83	6.62	6.74	7.01	1

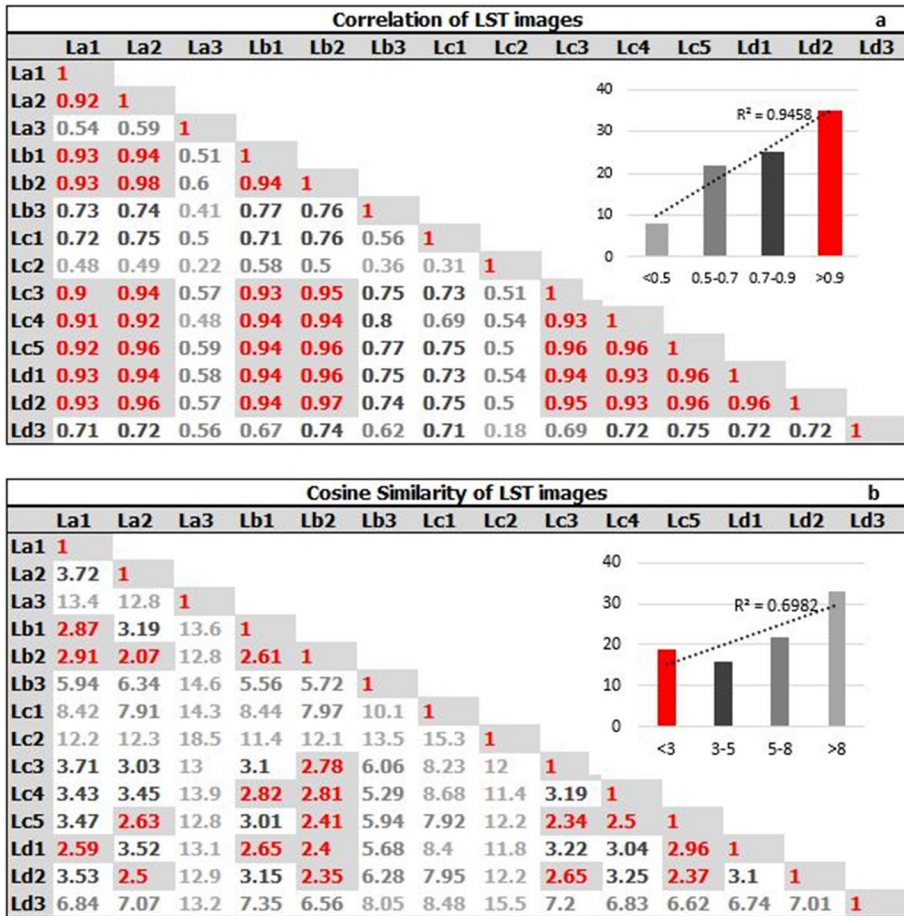$R^2 = 0.6982$ (bar chart categories: <3, 3-5, 5-8, >8)

Fig. 7 Assessment of dataset. **a** Correlation matrix o LST images, **b** cosine similarity o LST images

3.3 Datasets selection and evaluation

3.3.1 Datasets selection

The datasets to be used in the study were determined by correlation (Fig. 7a) and cosine similarity (Fig. 7b) to eliminate the errors of visual assessment. For this, the sub-study region was taken into consideration.

The correlations between the values of the LST images were also assessed because just the greatest and lowest values can produce misleading findings when showing the relationships between the images (Fig. 6a).

When Fig. 7a is analyzed, it becomes obvious that the La2, Lb2, and Ld2 images, where the shutdown takes place, have extremely strong correlations between their LST values. The Lc2 image showed a respectable degree of association with other images. The La3 image showed a weak correlation, it was noticed after examining the relationships of the other images.

Cosine similarity, one of the similarity distance approaches often used in machine learning and data mining studies, was also used between the data in order to support the correlation results and to decrease the error factor. The cosine result value or the angle in the cosine similarity method determines how similar the data are. The angle values between the vector values are shown in the table in order to better analyze the results because the Cosine result value in the study is extremely close to each other (Fig. 7b).

The degree of similarity between two sets of data increases as the angle between them decreases. The Lb1 and Lb2 images have a similarity of 2.61, which is the highest. Ld1 and Ld2 are the next images, followed by La1 and La2 with 3.10 and 3.72, respectively, then Lb2 and Lb3 with 5.72. The resemblance of the images to one another reduces as the angular magnitudes rise. Also, the study looked at the similarities between images from the closure period and those from other time periods.

With values of 2.07 and 2.50, respectively, it is feasible to claim that La2 is relatively comparable to Lb2, Ld2, when the similarities between the images taken during the closing periods are assessed. With a value of 2.35, Lb2 is likewise pretty comparable to Ld2. Lc2 was found to deviate significantly from all of the data.

Nine images, three of which are before closure (La1, Lb1, Ld1), three of which are during closure (La2, Lb2, Ld2), and three of which are after closure (Lc3, Lc4, Lc5), have angular similarity values in the range of 0–5. Twelve images are used, 4 of which are before closure (La1, Lb1, Lc1, Ld1), 3 of which are during closure (La2, Lb2, Ld2), and 5 of which are after closure (Lb3, Lc3, Lc4, Lc5, Ld3) it falls between 0 and 10. In the analysis, two images with angular values larger than 10 were disregarded.

By comparing the LST values of large impermeable architectural structures, La1, Lb1, and Ld1 images could be used for pre-covid shutdown to evaluate La2, even at different periods, to support the study. La2, Lc3, Lc4, and Lc5 images could all be analyzed post-COVID-19.

La1, Lb1, Ld1 images for pre-Covid and Lc3, Lc, and Lc5 images for post-COVID-19 were examined for Lb2 time.

It was impossible to find an image that could be utilized to calculate Lc2 time. This image has unusually high angular values at all other times.

La1, Lb1, and Ld1 might be utilized to determine Ld2 time for pre-Covid. Lc3, Lc4, and Lc5 images for the post-COVID-19 periods could be assessed.

A total of 12 images were determined as a result of all of these assessments. It was agreed to use La1, Lb1, Lc1, and Ld1 images in the pre-COVID-19 periods, La2, Lb2, and Ld2 images in the closure periods, and Lb3, Lc3, Lc4, Lc5, Ld3 images in the post-COVID-19 phase of showing the consequences of the pandemic.

3.3.2 OLS evaluation

In addition, the correlations between the LSTs predicted by the OLS method utilizing these values, as well as the biophysical effects NDVI, NDBI, and albedo, which are among those determining the LST value, were looked at.

Raster to pixel method was used to construct the pixels in this region, and LST, LULC, NDVI, NDBI, and albedo values were assigned to each pixel.

Unfortunately, the high density of pixels in the work area ultimately decreases the computer's speed and complicates processing. For this reason, a minimum of 58,942 samples was selected, with the sampling technique taking into account the 99% confidence interval

Table 6 OLS Results of samples

Dataset	Ilk sayı	NDBI	NDVI	Albedo	Adjusted R^2
La1	33.433	6.1104	− 1.8473	14.2291	0.80
La2	27.8936	4.2088	− 14.0514	8.4746	0.79
Lb1	33..3098	5.7459	− 12.4174	11.9931	0.78
Lb2	33.3673	6.6608	− 13.5023	7.8589	0.79
Lb3	27.3167	26.8211	0.0991	14.6608	0.49
Lc1	35.6813	27.0186	0.3299	− 32.1035	0.64
Lc3	32.9798	8.9364	− 10.8859	− 5.0303	0.74
Lc4	35.9710	8.0938	− 13.1182	9.5465	0.74
Lc5	34.9609	7.8659	− 13.2902	2.2964	0.80
Ld1	39.4415	6.6612	− 14.8070	2.9483	0.83
Ld2	32.6283	6.5588	− 13.3807	1.4899	0.81
Ld3	38.1235	35.0366	2.6193	− 36.9705	0.53

and the 0.5% margin of error, and 60,000 points were employed in the study. The homogeneity of these points throughout the study area was taken into consideration.

Also, the OLS algorithm was applied to these numbers to reveal anticipated LST values (Table 6).

Lb3 and Ld3 were found to have the lowest Adjusted r2 values. Lc1 is the dataset that comes after these. The NDBI coefficient values showed an excess when the OLS result formulations were looked at. Contrary to expectations, NDVI readings, on the other hand, display a favorable association with LST. The coefficients of albedo values in these datasets also showed an extraordinary difference. This circumstance should therefore be considered in the evaluation procedures that will use these images.

In correlation and cosine similarity evaluations, Lb3, Lc1, and Ld3 images with low R2 values show average and poor similarity structure. It also displays parallelism with these assessments. These images' NDBI and NDVI readings likewise indicated very unusual results. A positive association between LST and NDBI is normally predicted, although estimates of the NDBI coefficient are thought to be greatly overestimated.
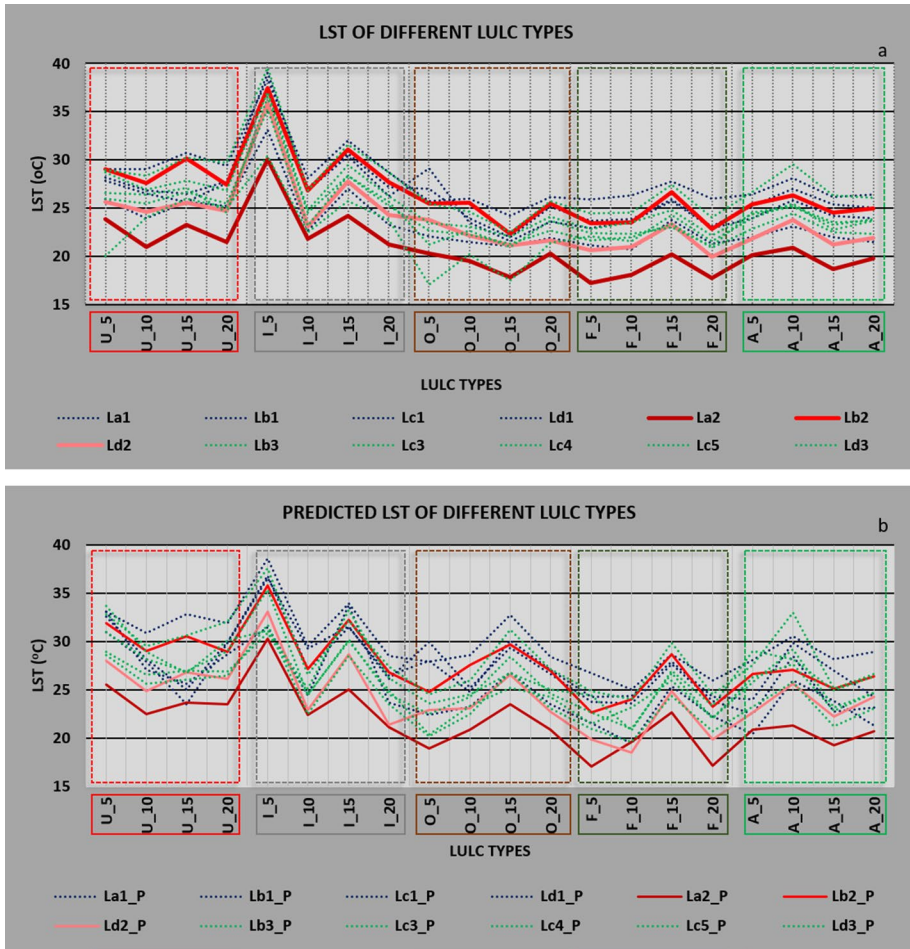
3.3.3 Analyzing of selected LST and predicted LST dataset values of different LULC

LST and predicted LST graphs for comparison have been created using pixels from the 5th, 10th, 15th, and 20th land-use categories. The analyzing between LST (Fig. 8a), predicted LST (Fig. 8b) and LULC in the chosen study location was examined at in order to compare these images with each other because the study's goal is to monitor artificially impervious significant surface temperature variations in areas with considerable human movement.

As a result, the COVID-19 shutdown periods are colder than other periods. Except for the Lb2 image in urban areas, lower La2 and Ld2 values were detected as compared to other times. This is true for industrial and other man-made places. As expected, forest and agricultural areas have lower LST values than other locations. Furthermore, 2–3 C standard deviations are found during the shutdown time. However, a constant state is not observed in urban or industrial settings. Temperatures dropped from 27 degrees to 25.5 degrees Celsius during the closing times (Fig. 5a).

In the study, LSTs were predicted using the OLS approach, which took into consideration the biophysical factors influencing surface temperatures. Their results are interpreted for the

Fig. 8 Analyzing selected data values. **a** LST. **b** Predicted LST values and LULC types

same pixels as well. As a result, the 5th Pixel of the City Areas has comparable characteristics to the LST; however, the surface temperature values are significantly higher here. More erratic outcomes were achieved as a result of these calculations. This demonstrates the influence of biophysical variables in the region (Fig. 5b). However, as shown in both graphs, surface temperatures have decreased over the period of COVID-19 shutdown.

3.4 Big architectural structures results

In this part, taking into account the assessments provided for the study area's chosen sub-region, it is shown how it was impacted by the major event during the COVID-19 closure period using both a visual method and a cosine similarity technique.

3.4.1 Selected LST dataset presentation for visual evaluation

Eight separate massive impermeable surfaces' LST maps were created, and they were visually interpreted (Fig. 9).

Before the COVID-19 closure, Akyaka Park Shopping Mall (AP SM) unexpectedly displays a surface temperature shift of up to 45–50 degrees, unlike other structures, yet it appears to be at rest in the subsequent times. During the COVID-19 closure period, Icerenkoy Shopping Mall (IC SM) surface temperatures decreased as seen in La2 and Ld2 pictures. Yet, LST values are still present because it has a Carrefour for basic purchases. Particularly prior to the COVID-19 shutdown, Viaport (V SM) appears to be significantly more active. Among the structures with green roofs are Ring Shopping Mall (R SM), Akasya (A SM), and others. Here, it is easy to discern that heating and cooling systems, which exhibit certain characteristics in other places, are completely absent. The mall that best represents the COVID-19 closure is Meydan Mall (M SM). Throughout COVID-19, the Modoko Furniture Site (M F) remained closed. With some limitations, Sabiha Gökçen Airport (SG A) has offered service throughout. The visual method, however, is insufficient to assess this circumstance. We looked at similarities for these structures.

3.4.2 Selected LST dataset cosine similarity

After the images were deleted, evaluation of the 12 remaining images was done in this section. The evaluations employed LST data from major building structures. One by one, the percentages of the images of each construction block that were comparable to one another were calculated (Fig. 10).

Before COVID-19 only shows the similarities of the images before the COVID-19 shutdown (La1-Lb1, Lb1-Lc1, Lc1-Ld1, etc.). Before and after COVID-19 shows the similarities of the images of these times with each other (Lb1-Lc4, Lb3-Lc1, etc.). After COVID-19 reveals the similarities of the images after the end of the shutdown (Lc3-Lc4, Lb3-Lc5, etc.). During COVID-19 reveals the results in this period (La1-La2, Lb2-Ld2, Ld2-Ld3 etc.).

While categorizing angular similarity values, Very Low similarity for values > 4, Low similarity for values 4–3, Moderate similarity for values 3–2, Strong similarity for values 2–1, and Very Low similarity for values 1 were assessed.

There were 528 distinct combination cases in total. The COVID-19 closure is covered by 240 of these, followed by 48 pre-COVID-19, 160 pre-COVID-19 and post-COVID-19, and 80 post-COVID-19.

The similarity rates of all places and significant architectural structures have also been calculated and are shown in Table 7.

The relationships between each image of a point that belonged to the chosen architectural structures were assessed. Images from the COVID-19 era had high similarity and high similarity percentages, with values of 18.56% and 17.05%, respectively. On the other hand, the images taken before and after the COVID-19 shutdown show a significant similarity of 11.93%.

As compared to other shopping malls, the Akasya mall has a high similarity rate of 3.03% before and before the COVID-19 closure and 3.22% during the COVID-19 period. After COVID-19, Akasya Park SM's high similarity decreased to 1.52% from 3.60% during that time. All shopping malls display comparable results in this. The only location with low and extremely low similarities is Sabiha Gökçen Airport.
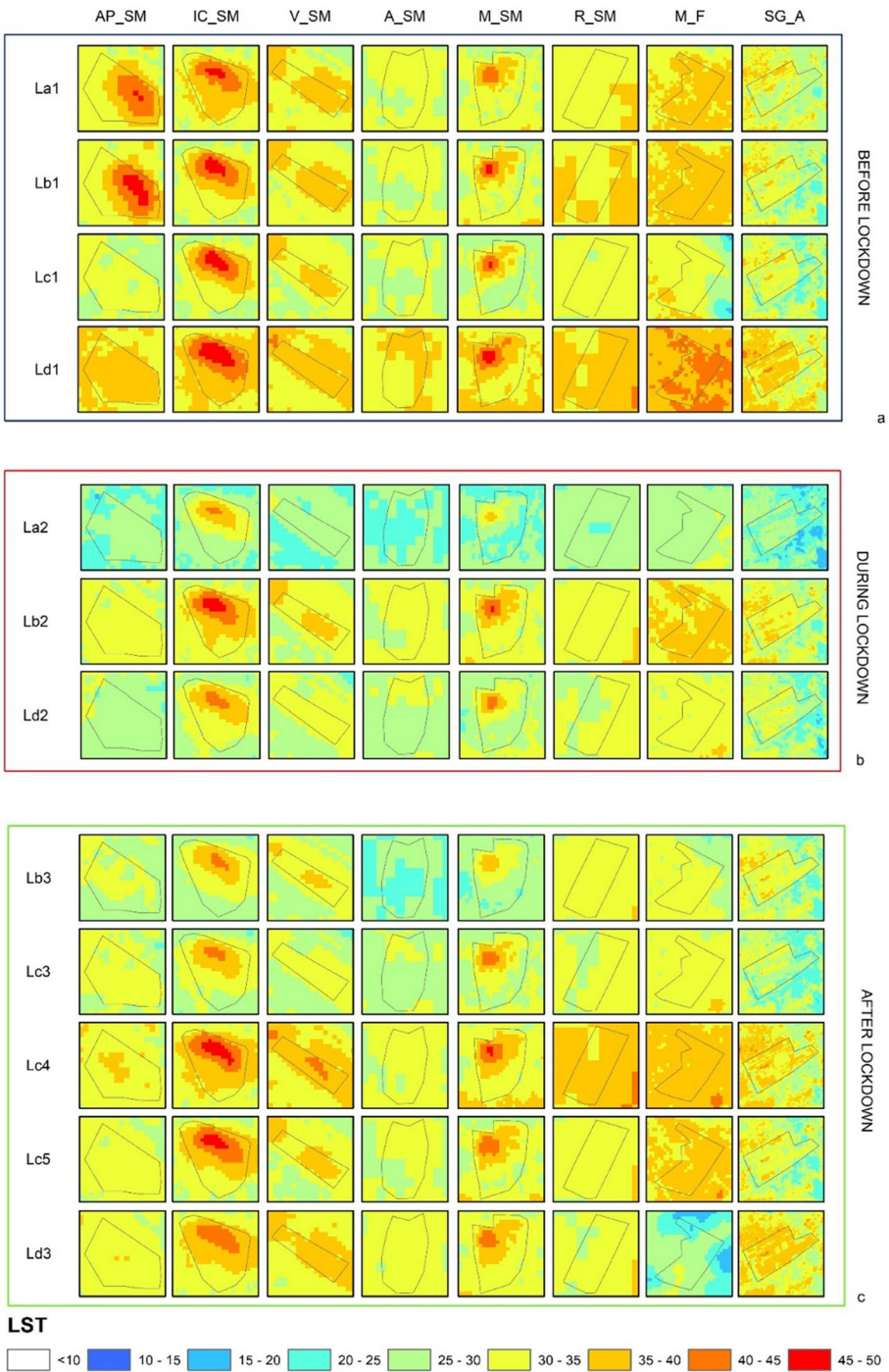
Fig. 9 LST values of big structures. **a** Before lockdown. **b** During lockdown. **c** After lockdown

BIG ARCHITECTURAL STRUCTURES AND SIMILARTY DISTRUBITION (%)
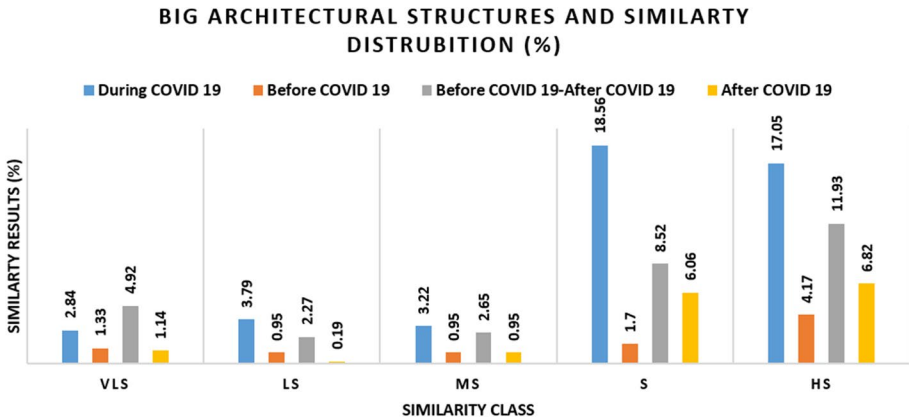
Fig. 10 Similarity results of whole structures

Table 7 Similarity percentage

		SUM	A_SM	AP_SM	R_SM	IC_SM	M_F	M_SM	SG_A	V_SM
VLS	DC	2.84	0.00	1.14	0.00	0.00	0.57	0.00	1.14	0.00
	BC	1.33	0.00	0.76	0.00	0.00	0.00	0.00	0.57	0.00
	BC-AC	4.92	0.00	1.89	0.00	0.00	0.76	0.00	2.27	0.00
	AC	1.14	0.00	0.00	0.00	0.00	0.76	0.00	0.38	0.00
LS	DC	3.79	0.00	0.00	0.00	0.00	0.57	0.00	3.22	0.00
	BC	0.95	0.00	0.00	0.00	0.00	0.57	0.00	0.38	0.00
	BC-AC	2.27	0.00	0.00	0.00	0.00	0.57	0.19	1.52	0.00
	AC	0.19	0.00	0.00	0.00	0.00	0.00	0.00	0.19	0.00
MS	DC	3.22	0.00	0.00	0.00	1.14	0.38	0.57	1.14	0.00
	BC	0.95	0.00	0.00	0.00	0.57	0.00	0.38	0.00	0.00
	BC-AC	2.65	0.00	0.00	0.00	1.14	0.76	0.76	0.00	0.00
	AC	0.95	0.00	0.00	0.00	0.00	0.00	0.19	0.76	0.00
S	DC	18.56	2.46	3.60	1.33	4.55	0.19	5.11	0.19	1.14
	BC	1.70	0.00	0.19	0.00	0.38	0.00	0.76	0.19	0.19
	BC-AC	8.52	0.76	0.76	1.14	2.46	0.00	2.84	0.00	0.57
	AC	6.06	0.76	0.38	0.38	1.70	0.57	1.52	0.57	0.19
HS	DC	17.05	3.22	0.95	4.36	0.00	3.98	0.00	0.00	4.55
	BC	4.17	1.14	0.19	1.14	0.19	0.57	0.00	0.00	0.95
	BC-AC	11.93	3.03	1.14	2.65	0.19	1.70	0.00	0.00	3.22
	AC	6.82	1.14	1.52	1.52	0.19	0.57	0.19	0.00	1.70

The values of 12 images from the 5th, 10th, 15th, and 20th pixels of big architectural structures were compared based on the analytical results stated above (Fig. 11).

A few specific structures like İçerenköy Shopping Mall and Meydan Shopping Mall, it is evident that the LST values during the COVID-19 shutdown periods are lower than most of the previous and following periods in all other large buildings (Fig. 11). Due to
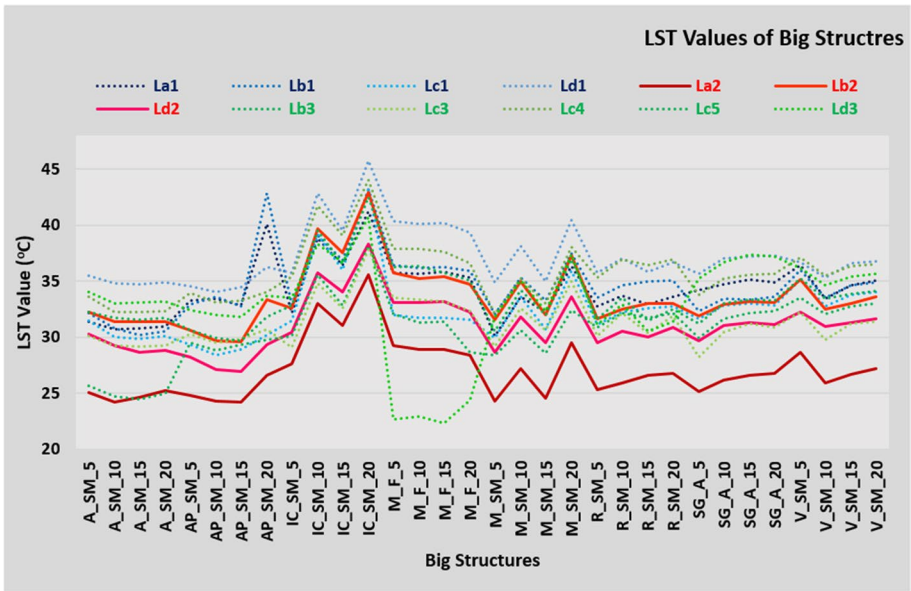
Fig. 11 LST values of big structures

the restriction on human mobility in massive structures during the shutdown period, this condition may have contributed to the large heating and cooling systems failing.

The margin of error in the chart must be considered because the chosen pixels reveal random locations for massive structures, which is one of the study's limitations.

The possibility of cloud in the area, which directly impacts the surface temperatures, is one of the study's other limiting variables. It was quite challenging to work because the closure time fell during the spring months and the study region was situated during the rainy season.

Also, although the variations in the year and day produce some changes in the surface temperatures, the findings of the correlation analysis and the similarity analysis indicate that the images have a limited use.

3.5 Google Mobility Index results

The regions with big architectural structures inside their borders presented results from the Google Mobility Index (Table 8).

When the table is assessed, all fields—with the exception of residential areas—show negative values. These findings demonstrate the slowing of mobility.

4 Discussion

Our social life has undergone considerable modifications as a result of the COVID-19 regulations. Restrictions have also had an impact on our daily mobility. Our surroundings have changed significantly as a result of this scenario. Many changes, from surface temperature

Table 8 Google Mobility Index Results

Area	Atasehir				Pendik				Umraniye				Uskudar			
	April		May		April		May		April		May		April		May	
	12	28	14	30	12	28	14	30	12	28	14	30	12	28	14	30
R&R	−98	−64	−55	−90	−97	−54	−44	−89	−97	−60	−53	−91	−98	−73	−66	−91
G&P	−97	10	15	−65	−94	11	18	−58	−96	13	21	−63	−97	7	13	−59
P	−88	−23	19	−77	−93	−33	−2	−88	−92	−42	−17	−80	−93	−44	−18	−83
TS	−91	−51	−39	−81	−95	−70	−66	−89	−95	−57	−44	−86	−94	−62	−53	−89
W	−84	−56	−46	−69	−78	−44	−36	−58	−82	−52	−43	−69	−83	−60	−51	−73
R	29	25	22	34	28	21	18	31	29	24	20	34	27	26	22	32

* R&R: Retail&Recreation, G&P: Grocery&Pharmacy, TS: Transit Stations, P: Parks, W: Workplaces, R: Residential

changes to changes in air quality, have been observed, albeit for a short time, as a result of the lengthening of our stays in our homes but the restriction of mobility in public places to stop the pandemic from spreading. Numerous studies have been conducted on these changes.

The Anatolian side of Istanbul, which lies inside its provincial boundaries, is the subject of this study. It was looked at how the COVID-19 period affected the values of the land surface temperature in this area. Additionally, it has been considered how the closure may effect the surface temperatures of substantial buildings located inside these bounds.

First of all, the 2018 CORINE data collection was used to calculate the impermeable surfaces of Istanbul's Anatolian Side (Fig. 3), as in earlier research (Stathopoulou et al., 2007; Walawender et al., 2014). The results show that urban fabric areas like dwelling, business, industry, healthcare, and public buildings have the highest percentage distribution of artificial surfaces (55.89%).

Shopping centers and industrial sites make up the discontinuous urban fabric areas, which comprise 32.29% of the region's impermeable surfaces and have a dominant land-use pattern (Table 3). These types of structures can be found in the area, including shopping centers and the Modoko Furnishers Site.

The major airport on the Anatolian side of Istanbul, Sabiha Gokcen Airport, occupies 1.15% of the city and is one of its most significant logistics and distribution hubs. Airports, shopping malls, and industrial sites all have characteristics that influence their local climates (Chen et al., 2020; Murphy, 2015; Trlica et al., 2017; Wardana, 2015; Zaeemdar & Baycan, 2017). The study concentrates on various significant shopping malls, Modoko Furnishers Site, and Sabiha Gokcen Airport as a consequence.

As a result of COVID-19, which started in 2020, all nations have implemented various measures. Studies show that the COVID-19 closure has decreased surface temperatures. Our work evaluated LST variations, just like earlier studies (Arrofiqoh & Setyaningrum, 2021; Ghosh et al., 2020; Marvi et al., 2021; Taoufik et al., 2021; Teufel et al., 2021) that noted urban temperature changes as a result of COVID-19. We used 14 LANDSAT 8 OLI/TIRS satellite images from 2016 and 2022 to calculate the LST values.

The temperature drops in some locations have been noticed as a result of high-density forest areas, despite zoning status changes and the establishment of new dense urbanization zones on the Anatolian side of Istanbul, whose effects on urbanization have not yet been seen (Fig. 4). These regions remain in the northern parts of the Anatolian side. The temperatures in these regions before and after COVID-19 appear to be between 20–25 and 30–35 °C (Fig. 4a, b, g, l, c, I, n, j, k). During the periods of COVID-19 closures, the 15-20, 20–25 °C ranges are interpreted visually (Fig. 4b, e, h, m).

In metropolitan areas, the values concentrated as 35–40, 40–45, and > 45 are concentrated at 25–30, 30–35-35–40 C in the COVID-19 limits if these regions are located on the south shore of the Anatolian Side. Local temperature increases are often observed in Kadikoy, Maltepe, Pendik, and Tuzla. Furthermore, these are the general locations of residential districts. Local temperature rises have been observed in Umraniye, Sancaktepe, Atasehir, and Sultanbeyli districts, which are home to urban neighborhoods rather than commercial areas (Fig. 4o). This could be explained by the increased time spent indoors due to the COVID-19 regulations, as well as the widespread use of artificial cooling and heating components. When the images are studied separately, the cloud closure is extremely intense in early May during the COVID-19 shutdown period (Fig. 4h) and in early April following the COVID-19 shutdown (Fig. 4c). The clouds are concentrated in the northeast of the region in the images taken at the end of April after the shutdown. Because this condition is not in the sub-study area, it has little effect on the surface temperature values.

When we look at the sub-study region's land-use and land cover average surface temperature values, we can talk about an average value that is not very varied before the closure in urban areas (Fig. 5). Until recently, changes in cities, industrial regions, and other artificial surfaces were mainly observed at 28–33 degrees. Except for the late April period (Lb2), the situation in such land uses decreased to 23–28 degrees during the Covid closure periods. Given that the cloud impact may affect surface averages in average valleys, surface temperatures were also examined in the study based on land-use status. Figure 6 clearly shows that the surface temperature values, which are 25–35 degrees, range between 20 and 30 degrees.

The declines throughout this period parallel the changes observed in Bacak et al., 2020 works for Istanbul. In their research, they claimed that there was a correlation between a decrease in air pollution and temperature (Bacak et al., 2020).

Because visual evaluation of the study's accuracy and sensitivity may not be sufficient, correlation and cosine similarity methodologies were also included in the investigation.

The correlation values between 14 images (Fig. 7a) and cosine similarity (Fig. 7b) were also investigated. As a result, high correlation values were discovered between the images. However, La3 and Lc2 images with correlation coefficients less than 0.50, which could create reluctance in the study, were removed. The cosine similarity method, which is utilized in many disciplines like picture clustering and text mining, is also employed to aid in the elimination process. Weak similarities between La3 and Lc2 pictures were found in this analysis.

OLS values were utilized to analyze the images used in this investigation, not only in relation to the surface temperature values, but also in relation to the biophysical parameters influencing the LST. The OLS model has been utilized in studies investigating the impact of biophysical factors on LST, such as NDVI, NDBI, and NDWI (Firozjaei et al., 2019; Roy et al., 2016; Wang et al., 2020; Zhou & Wang, 2011). In this manner, significantly more accurate evaluations of both the study area's surface temperature and big architectural buildings might be made. The results of this research reflect the findings of correlation and cosine similarity. As a result, Lb3, Lc1, and Ld3 images were discovered, which may cause secondary distress. Contrary to predictions, the NDBI values in the images are intermittently high, and the NDVI values are positive. These were also considered in the comments.

According to OLS findings, there is a negative association between NDVI and LST values, much like in other papers, and a positive correlation with NDBI and LST values (Guha et al., 2018; Khorrami & Gunduz, 2020) (Table 5). The closure periods have lower NDBI coefficients than certain other times. A lower NDVI coefficient was found when the NDVI coefficients were studied in comparison with some images. When the charts of the observed LST results and predicted LST results are examined, identical outcomes are observed simultaneously. Low values are seen in both systems during the closure times (Fig. 5a, b).

This study, unlike other studies, focuses on shopping malls, the Modoko industrial site, and Sabiha Gokcen Airport, which are some of the architectural structures that occupy a large physical space, to compare temperature changes related to the restriction of human mobility with artificial air conditioning in COVID-19 closures. Additionally, declines are seen during the COVID-19 closure periods, citing the Google Mobility Index statistics. In the second section of the study, which evaluates big architectural structures during the COVID-19 period, a decline in the surface temperature values of the Icerenkoy Shopping Mall is seen.

The LST decreases during the shutdown period in major buildings (Fig. 11) are also supported by the Google Mobility Index results (Table 7) from the same days.

5 Conclusion

According to the studies, due to population expansion, immigration, and uneven structuring, Istanbul's impermeable surfaces are constantly expanding. Surface temperatures change as the number of impermeable surfaces rises. However, unlike previous studies, this one used a number of methods to determine whether or not there was a link between temperature differences in large architectural structures and COVID-19 closures, even while impermeable surfaces and green spaces did not vary considerably. According to the findings of this study, even when the city's daily bustle slows down temporarily, the surface temperatures of the metropolis still change. These elements have been included into huge architectural projects, particularly when artificial air conditioning changes are used. During the COVID-19 closures, one of these large architectural complexes, shopping malls, has marketplaces open where only urgent and basic requirements are met. As a result, they were taken into account in the evaluation by determining if these markets were open during the relevant period.

In total, 14 satellite images were utilized to create LST maps, which were then visually inspected, in order to investigate this scenario. The LST maps were then removed using both correlational and similarity techniques. The technique for establishing the relationship between variations in surface temperature before, during, and after the closure of COVID-19 and land utilization was carried out. During these eras, the relationship between land usage and LST levels was discovered to be acceptable. In order to support the study, the biophysical parameters that affect the LST were also evaluated, as were the LST values predicted using the OLS technique. In light of these findings, an analysis of large architectural structures has begun.

The Anatolian Side of Istanbul, which is quickly developing, has a large number of shopping complexes to meet the shopping and purchasing needs of its population. There is also a big furniture manufacturing factory in this area, as well as Sabiha Gökçen Airport, which handles many international flights. LST values were evaluated using the similarity results provided to analyze variations in the LST values of these places during the COVID-19 era in comparison with earlier times. LST values in these regions were found to be lower in the COVID-19 period when compared to earlier periods.

These shutdown policies have generated a number of economic and social concerns, and they will have a long-term impact on how we live. The authors of this study emphasize that, despite its drawbacks, the shutdown should be seen as a success in terms of environmental assessments, and that the best course of action should be thoroughly investigated.

The combination of socioeconomic, topographic, and environmental components in the following approach, in addition to the biophysical aspects impacting the LST used in the study, is expected to boost such research. Furthermore, using MODIS day and night images, the technique can be broadened to include images with low spatial resolution but high temporal resolution. Furthermore, by lowering the role of the human player in such investigations, tools such as machine learning and artificial intelligence will aid in automatic decision making.

Author contributions L.K. analyzed and visualized; L.K. and U.F.K considered the research materials, conducted a field survey, reviewed and edited together in this study.

Data availability The datasets generated during and/or analyzed during the current study are available from the corresponding author on reasonable request.

Declarations

Conflict of interest The authors declare that they have no known competing financial interests or personal relationships that could have appeared to influence the work reported in this paper.

References

Ahn, H., Lee, S., Ko, H., Kim, M., Won, S., & Seok, J. (2023). Searching similar weather maps using convolutional autoencoder and satellite images. *ICT Express, 9*(1), 69–75. https://doi.org/10.1016/j.icte.2022.03.013

Almeida, R. D., & Cl, A. (2021). Study of the urban heat island (uhi) using remote sensing data/techniques: A systematic review. *Environments, 8*(105), 1–39.

Alqasemi, A. S., Hereher, M. E., Kaplan, G., Al-quraishi, A. M. F., & Saibi, H. (2021). Science of the total environment impact of COVID-19 lockdown upon the air quality and surface urban heat island intensity over the United Arab Emirates. *Science of the Total Environment, 767*, 144330. https://doi.org/10.1016/j.scitotenv.2020.144330

Arik, A. O., & Çavdaroğlu, G. Ç. (2023). Istanbul's community mobility changes during the COVID-19 pandemic: A spatial analysis. *Journal of Data Applications, 1*(1), 1–18. https://doi.org/10.26650/JODA.1215566

Arrofiqoh, E. N., & Setyaningrum, D. A. (2021). The impact of Covid-19 pandemic on land surface temperature in Yogyakarta urban agglomeration. *Journal of Applied Geospatial Information, 5*(1), 480–485. https://doi.org/10.30871/jagi.v5i1.2784

Avdan, U., & Jovanovska, G. (2016). Algorithm for automated mapping of land surface temperature using LANDSAT 8 satellite data. *Journal of Sensors.* https://doi.org/10.1155/2016/1480307

Bacak, T. N., Dursun, Ş, & Toros, H. (2020). The effect of COVID-19 outbreak on air quality of istanbul city centre the effect of COVID-19 outbreak on air quality of Istanbul city centre. *Journal of Research in Atmospheric Science, 2*(1), 7–11.

Balçik, S., Kilinç, C., Karaoğlu, G., & Yamaçli, R. (2021). Covid- 19 Salgınının Kentsel Yaşama Etkileri: Türkiye Örneği effects of the Covid-19 pandemic on urban life: Turkish Case. *Mimarlık ve Yaşam Dergisi (Journal of Architecture and Life), 6*(3), 1081–1095. https://doi.org/10.26835/my.883439

Baryła, A., Karczmarczyk, A., Bus, A., & Witkowska-Dobrev, J. (2019). Surface temperature analysis of conventional roof and different use forms of the green roof. *Scientific Review Engineering and Environmental Sciences, 28*(4), 632–640. https://doi.org/10.22630/PNIKS.2019.28.4.57

Başeğmez, M., & Aydın, C. C. (2021). Türkiye'de COVID-19 sürecinde alınan önlemler bakımından okul bahçelerinin ve sınıflarının CBS ile değerlendirilmesi. *Geomatik, 7*(3), 209–219. https://doi.org/10.29128/geomatik.971403

Baysan, C., Palanbek Yavaş, S., & Çöl, M. (2021). Change in air pollution and human mobility trends during COVID-19 lockdown measures in Turkey. *The Anatolian Journal of Family Medicine, 4*(2), 170–177. https://doi.org/10.5505/anatoljfm.2021.25338

BİMTAŞ. (2020). *Covid-19 salgini mücadele sürecinde istanbul kirilganlik haritasi proje raporu.* İstanbul, Kasım 2020.

Büttner, G., Kosztra, B., Maucha, G., Patak, R., Kleeschulte, S., Hazeu, G., & Littkopf, A. (2021). *CORINE Land Cover Product User Manual (Version 1.0). Copernicus Land Monitoring Service.* https://land.copernicus.eu/user-corner/technical-library/clc-product-user-manual

Cai, Z., Tang, Y., & Zhan, Q. (2021). A cooled city? Comparing human activity changes on the impact of urban thermal environment before and after city-wide lockdown. *Building and Environment, 195*, 107729. https://doi.org/10.1016/j.buildenv.2021.107729

Cao, Q., Liu, Y., Georgescu, M., & Wu, J. (2020). Impacts of landscape changes on local and regional climate: A systematic review. *Landscape Ecology, 35*(6), 1269–1290. https://doi.org/10.1007/s10980-020-01015-7

Chakraborty, T., Sarangi, C., & Lee, X. (2021). Reduction in human activity can enhance the urban heat island: Insights from the COVID-19 lockdown. *Environmental Research Letters, 16*(5), 054060. https://doi.org/10.1088/1748-9326/abef8e

Charlton, M., & Fotheringham, A. S. (2009). *Geographically Weighted Regression White Paper.*

Chen, H. C., Han, Q., & De Vries, B. (2020). *Modeling the spatial relation between urban morphology, land surface temperature and urban energy demand. Sustainable Cities and Society*. Elsevier.

Cristóbal, J., Jiménez-Muñoz, J. C., Prakash, A., Mattar, C., Skoković, D., & Sobrino, J. A. (2018). An improved single-channel method to retrieve land surface temperature from the landsat-8 thermal band. *Remote Sensing*. https://doi.org/10.3390/rs10030431

Dhyani, Y., & Pandya, R. J. (2021). Deep Learning Oriented Satellite Remote Sensing for Drought and Prediction in Agriculture. In *2021 IEEE 18th India Council International Conference (INDICON)* (pp. 1–5). Guwahati, India: IEEE. https://doi.org/10.1109/INDICON52576.2021.9691608

Do Nascimento, A. C. L., Galvani, E., Gobo, J. P. A., & Wollmann, C. A. (2022). Comparison between air temperature and land surface temperature for the city of São Paulo, Brazil. *Atmosphere, 13*(3), 1–21. https://doi.org/10.3390/atmos13030491

Efe, B. (2022). Air quality improvement and its relation to mobility during COVID - 19 lockdown in Marmara Region, Turkey. *Environmental Monitoring and Assessment*. https://doi.org/10.1007/s10661-022-09889-7

El Kenawy, A. M., Lopez-Moreno, J. I., McCabe, M. F., Domínguez-Castro, F., Peña-Angulo, D., Gaber, I. M., Alqasemi, A. S., Al Kindi, K. M., Al-Awadhi, T., Hereher, M. E., & Robaa, S. M. (2021). The impact of COVID-19 lockdowns on surface urban heat island changes and air-quality improvements across 21 major cities in the Middle East. *Environmental Pollution, 288*, 117802. https://doi.org/10.1016/j.envpol.2021.117802

Firozjaei, M. K., Alavipanah, S. K., Liu, H., Sedighi, A., Mijani, N., Kiavarz, M., & Weng, Q. (2019). A PCA-OLS model for assessing the impact of surface biophysical parameters on land surface temperature variations. *Remote Sensing*. https://doi.org/10.3390/rs11182094

Gallo, K., Hale, R., Tarpley, D., & Yu, Y. (2011). Evaluation of the relationship between air and land surface temperature under clear- and cloudy-sky conditions. *Journal of Applied Meteorology and Climatology, 50*(3), 767–775. https://doi.org/10.1175/2010JAMC2460.1

U.S. Geological Survey. (2019). Landsat 8 Data Users Handbook. *Nasa, 8*(November), 114. https://landsat.usgs.gov/documents/Landsat8DataUsersHandbook.pdf

Ghosh, S., Das, A., Hembram, T. K., Saha, S., Pradhan, B., & Alamri, A. M. (2020). Impact of COVID-19 induced lockdown on environmental quality in four Indian megacities Using Landsat 8 OLI and TIRS-derived data and Mamdani fuzzy logic modelling approach. *Sustainability (switzerland), 12*(13), 1–24. https://doi.org/10.3390/su12135464

Google. (2022). COVID-19 Community Mobility Report. https://www.google.com/covid19/mobility/

Guerri, G., Crisci, A., Messeri, A., Congedo, L., Munafò, M., & Morabito, M. (2021). Thermal summer diurnal hot-spot analysis: The role of local urban features layers. *Remote Sensing, 13*(3), 538. https://doi.org/10.3390/rs13030538

Guha, S., & Govil, H. (2020). Seasonal contrast on the correlation between land surface temperature and normalized difference water index using a series of Landsat data. *International Journal of Engineering and Geosciences, 6*(3), 165–173. https://doi.org/10.26833/ijeg.821730

Guha, S., & Govil, H. (2021). COVID-19 lockdown effect on land surface temperature and normalized difference vegetation index. *Geomatics, Natural Hazards and Risk, 12*(1), 1082–1100. https://doi.org/10.1080/19475705.2021.1914197

Guha, S., Govil, H., Dey, A., & Gill, N. (2018). Analytical study of land surface temperature with NDVI and NDBIusing Landsat 8 OLI and TIRS data in Florence and Naples city, Italy. *European Journal of Remote Sensing, 51*(1), 667–678. https://doi.org/10.1080/22797254.2018.1474494

Jacobson, M. Z., & Ten Hoeve, J. E. (2012). Effects of urban surfaces and white roofs on global and regional climate. *Journal of Climate, 25*(3), 1028–1044. https://doi.org/10.1175/JCLI-D-11-00032.1

Jiang, Y., & Lin, W. (2021). A comparative analysis of retrieval algorithms of land surface temperature from landsat-8 data: A case study of Shanghai, China. *International Journal of Environmental Research and Public Health, 18*(11), 5659. https://doi.org/10.3390/ijerph18115659

Khorrami, B., & Gunduz, O. (2020). Spatio-temporal interactions of surface urban heat island and its spectral indicators: A case study from Istanbul metropolitan area. *Turkey. Environmental Monitoring and Assessment, 192*(6), 1–13. https://doi.org/10.1007/s10661-020-08322-1

Kosztra, B., Büttner, G., Hazeu, G., & Arnold, S. (2017). *Updated CLC illustrated nomenclature guidelines. European Environment Agency*. Environment Agency Austria; EAA Spittelauer Lände 5 1090 Wien Austria. https://land.copernicus.eu/user-corner/technical-library/corine-land-cover-nomenclature-guidelines/docs/pdf/CLC2018_Nomenclature_illustrated_guide_20190510.pdf

Kotan, B., & Erener, A. (2022). Seasonal analysis and mapping of air pollution (PM10 and SO2) during Covid-19 lockdown in Kocaeli (Turkey). *International Journal of Engineering and Geosciences, 8*(2), 173–187. https://doi.org/10.26833/ijeg.1111699

Külekçi, E. A. (2017). Geçmişten Günümüze Yeşil Çatı Sistemleri ve Yeşil Çatılarda Kalite Standartlarının Belirlenmesine Yönelik Bir Araştırma (Green Roof Systems from Past to Today And Study on The Determination of Quality Standards in the Green Roof). *ATA Planlama ve Tasarım Dergisi, 1*(1), 35–53.

Kusak, L., & Kucukali, U. F. (2018). Outlier detection of land surface temperature: Küçükçekmece Region. *International Journal of Engineering and Geosciences*. https://doi.org/10.26833/ijeg.404426

Lee, S., Ryu, Y., & Jiang, C. (2015). Urban heat mitigation by roof surface materials during the East Asian summer monsoon. *Environmental Research Letters*. https://doi.org/10.1088/1748-9326/10/12/124012

Lee, H., Lee, K., Kim, J. H., Na, Y., Park, J., Choi, J. P., & Hwang, J. Y. (2021). Local similarity siamese network for urban land change detection on remote sensing images. *IEEE Journal of Selected Topics in Applied Earth Observations and Remote Sensing, 14*, 4139–4149.

Li, D., Bou-Zeid, E., & Oppenheimer, M. (2014). The effectiveness of cool and green roofs as urban heat island mitigation strategies. *Environmental Research Letters*. https://doi.org/10.1088/1748-9326/9/5/055002

Liang, S., Shuey, C. J., Russ, A. L., Fang, H., Chen, M., Walthall, C. L., et al. (2003). Narrowband to broadband conversions of land surface albedo: II. Validation. *Remote Sensing of Environment, 84*(1), 25–41. https://doi.org/10.1016/S0034-4257(02)00068-8

Liu, L., & Zhang, Y. (2011). Urban heat island analysis using the landsat TM data and ASTER Data: A case study in Hong Kong. *Remote Sensing, 3*(7), 1535–1552. https://doi.org/10.3390/rs3071535

Liu, W., Feddema, J., Hu, L., Zung, A., & Brunsell, N. (2017). Seasonal and diurnal characteristics of land surface temperature and major explanatory factors in Harris County, Texas. *Sustainability (Switzerland)*. https://doi.org/10.3390/su9122324

Malik, M. S., Shukla, J. P., & Mishra, S. (2019). Relationship of LST, NDBI and NDVI using landsat-8 data in Kandaihimmat watershed, Hoshangabad, India. *Indian Journal of Geo-Marine Sciences, 48*(1), 25–31.

Martin, M. A., Ghent, D., Pires, A. C., Göttsche, F. M., Cermak, J., & Remedios, J. J. (2019). Comprehensive in situ validation of five satellite land surface temperature data sets over multiple stations and years. *Remote Sensing*. https://doi.org/10.3390/rs11050479

Marvi, M., Arfeen, A., Mehdi, M. R., & Rauf, Z. (2021). Investigating the impact of regional temperature on covid-19 pandemic during 2020. *Sustainability (switzerland), 13*(11), 1–27. https://doi.org/10.3390/su13115931

Mashhoodi, B. (2020). Land surface temperature and energy expenditures of households in the Netherlands: Winners and losers. *Urban Climate, 34*(January), 100678. https://doi.org/10.1016/j.uclim.2020.100678

Mukherjee, F., & Singh, D. (2020). Assessing land use-land cover change and its impact on land surface temperature using LANDSAT data: A comparison of two urban areas in india. *Earth Systems and Environment, 4*(2), 385–407. https://doi.org/10.1007/s41748-020-00155-9

Murphy, S. (2015). Assessing the effectiveness of extensive green roofs at improving environmental conditions in Atlanta, Georgia, 1–80.

Oh, J. W., Ngarambe, J., Duhirwe, P. N., Yun, G. Y., & Santamouris, M. (2020). Using deep-learning to forecast the magnitude and characteristics of urban heat island in Seoul Korea. *Scientific Reports, 10*(1), 1–13. https://doi.org/10.1038/s41598-020-60632-z

RG. (2020). *Organizasyonların Ertelenmesi, Genelge, 2020/3, Sayı: 3107*. Ankara.

Rongali, G., Keshari, A. K., Gosain, A. K., & Khosa, R. (2018). A mono-window algorithm for land surface temperature estimation from landsat 8 thermal infrared sensor data: A case study of the beas river basin, India. *Pertanika Journal of Science and Technology, 26*(2), 829–840.

Roshan, G., Sarli, R., & Grab, S. W. (2021). The case of Tehran ' s urban heat island, Iran: Impacts of urban ' lockdown ' associated with the COVID-19 pandemic. *Sustainable Cities and Society, 75*(August), 103263. https://doi.org/10.1016/j.scs.2021.103263

Roshan, G., Sarli, R., & Fitchett, J. M. (2022). Urban heat island and thermal comfort of Esfahan City (Iran) during COVID-19 lockdown. *Journal of Cleaner Production, 352*(March), 131498. https://doi.org/10.1016/j.jclepro.2022.131498

Roy, D. P., Kovalskyy, V., Zhang, H. K., Vermote, E. F., Yan, L., Kumar, S. S., & Egorov, A. (2016). Characterization of Landsat-7 to Landsat-8 reflective wavelength and normalized difference vegetation index continuity. *Remote Sensing of Environment, 185*, 57–70. https://doi.org/10.1016/j.rse.2015.12.024

Şahin, Ü. A. (2020). The effects of COVID-19 measures on air pollutant concentrations at urban and traffic sites in Istanbul. *Aerosol and Air Quality Research, 5*, 1874–1885. https://doi.org/10.4209/aaqr.2020.05.0239The

Scott, L. M., & Janikas, M. V. (2010). Handbook of applied spatial analysis. *Handbook of Applied Spatial Analysis*. https://doi.org/10.1007/978-3-642-03647-7

Sekertekin, A., & Bonafoni, S. (2020). Sensitivity analysis and validation of daytime and nighttime land surface temperature retrievals from landsat 8 using different algorithms and emissivity models. *Remote Sensing*. https://doi.org/10.3390/RS12172776

Sharifi, E., & Lehmann, S. (2014). Comparative analysis of surface urban heat island effect in central sydney. *Journal of Sustainable Development, 7*(3), 23–34. https://doi.org/10.5539/jsd.v7n3p23

Sharma, A., Conry, P., Fernando, H. J. S., Hamlet, A. F., Hellmann, J. J., & Chen, F. (2016). Green and cool roofs to mitigate urban heat island effects in the Chicago metropolitan area: Evaluation with a regional climate model. *Environmental Research Letters*. https://doi.org/10.1088/1748-9326/11/6/064004

Shen, H., Huang, L., Zhang, L., Wu, P., & Zeng, C. (2016). Long-term and fine-scale satellite monitoring of the urban heat island effect by the fusion of multi-temporal and multi-sensor remote sensed data: A 26-year case study of the city of Wuhan in China. *Remote Sensing of Environment, 172*, 109–125. https://doi.org/10.1016/j.rse.2015.11.005

Sobrino, J. A., Caselles, V., & Becker, F. (1990). Significance of the remotely sensed thermal infrared measurements obtained over a citrus orchard. *ISPRS Journal of Photogrammetry and Remote Sensing, 44*(6), 343–354. https://doi.org/10.1016/0924-2716(90)90077-O

Sobrino, J. A., & Jiménez-Muñoz, J. C. (2005). Land surface temperature retrieval from thermal infrared data: An assessment in the context of the Surface Processes and Ecosystem Changes Through Response Analysis (SPECTRA) mission. *Journal of Geophysical Research d: Atmospheres, 110*(16), 1–10. https://doi.org/10.1029/2004JD005588

Stathopoulou, M., Cartalis, C., & Petrakis, M. (2007). Integrating corine land cover data and landsat TM for surface emissivity definition: Application to the urban area of Athens. Greece. *International Journal of Remote Sensing, 28*(15), 3291–3304. https://doi.org/10.1080/01431160600993421

Tan, E. (2022). The long-term impact of COVID-19 lockdowns in Istanbul. *International Journal of Environmental Research and Public Health, 19*(21), 1–22. https://doi.org/10.3390/ijerph192114235

Taoufik, M., Laghlimi, M., & Fekri, A. (2021). Comparison of land surface temperature before, during and after the COVID-19 lockdown using landsat imagery: A case study of Casablanca city. *Morocco. Geomatics and Environmental Engineering, 15*(2), 105–120. https://doi.org/10.7494/geom.2021.15.2.105

Teufel, B., Sushama, L., Poitras, V., Dukhan, T., Bélair, S., Miranda-Moreno, L., et al. (2021). Impact of COVID-19-related traffic slowdown on urban heat characteristics. *Atmosphere, 12*(2), 1–13. https://doi.org/10.3390/atmos12020243

Trlica, A., Hutyra, L. R., Schaaf, C. L., Erb, A., & Wang, J. A. (2017). Albedo, land cover, and daytime surface temperature variation across an urbanized landscape. *Earth's Future, 5*(11), 1084–1101. https://doi.org/10.1002/2017EF000569

Uzkent, B., Sheehan, E., Meng, C., Tang, Z., Burke, M., Lobell, D., & Ermon, S. (2019). Learning to Interpret Satellite Images in Global Scale Using Wikipedia. *arXiv 2019*. https://doi.org/10.48550/arXiv.1905.02506

Venter, Z. S., Chakraborty, T., & Lee, X. (2021). Crowdsourced air temperatures contrast satellite measures of the urban heat island and its mechanisms. *Science Advances, 7*(22), 1–10. https://doi.org/10.1126/sciadv.abb9569

Walawender, J. P., Szymanowski, M., Hajto, M. J., & Bokwa, A. (2014). Land surface temperature patterns in the urban agglomeration of Krakow (Poland) derived from landsat-7/ETM+ data. *Pure and Applied Geophysics, 171*(6), 913–940. https://doi.org/10.1007/s00024-013-0685-7

Wang, Z., Fan, C., Zhao, Q., & Myint, S. W. (2020). A geographically weighted regression approach to understanding urbanization impacts on urban warming and cooling: A case study of Las Vegas. *Remote Sensing*. https://doi.org/10.3390/rs12020222

Wardana, I. K. (2015). Analysis of urban surface temperature for green spaces planning in Bandung city, Indonesia. *University of Twente, 1*, 593–605.

Wheeler, D. C. (2014). Geographically weighted regression. *Handbook of Regional Science*. https://doi.org/10.1007/978-3-642-23430-9_77

WHO. (2023). Search by Country Europe. *WHO Coronavirus (COVID-19) Dashboard*. https://covid19.who.int/

Zaeemdar, S., & Baycan, T. (2017). Analysis of the relationship between urban heat island and land cover in istanbul through landsat 8 OLI. *Journal of Earth Science & Climatic Change*. https://doi.org/10.4172/2157-7617.1000423

Zaragoza, A., & Bartolom, C. (2012). Albedo effect and energy efficiency of cities. *Sustainable Development - Energy, Engineering and Technologies - Manufacturing and Environment*. https://doi.org/10.5772/29536

Zhao, Q., Myint, S. W., Wentz, E. A., & Fan, C. (2015). Rooftop surface temperature analysis in an urban residential environment. *Remote Sensing, 7*(9), 12135–12159. https://doi.org/10.3390/rs70912135

Zhou, X., & Wang, Y. C. (2011). Dynamics of land surface temperature in response to land-use/cover change. *Geographical Research, 49*(1), 23–36. https://doi.org/10.1111/j.1745-5871.2010.00686.x

Zhou, Y., Weng, Q., Gurney, K. R., Shuai, Y., & Hu, X. (2012). Estimation of the relationship between remotely sensed anthropogenic heat discharge and building energy use. *ISPRS Journal of Photogrammetry and Remote Sensing, 67*(1), 65–72. https://doi.org/10.1016/j.isprsjprs.2011.10.007